

# 1 **Constraining Mass-Diameter Relations from Hydrometeor** 2 **Images and Cloud Radar Reflectivities in Tropical** 3 **Continental and Oceanic Convective Anvils**

4  
5 **E. Fontaine<sup>1</sup>, A. Schwarzenboeck<sup>1</sup>, J. Delanoë<sup>2</sup>, W. Wobrock<sup>1</sup>, D. Leroy<sup>1</sup>, R.**  
6 **Dupuy<sup>1</sup>, C. Gourbeyre<sup>1</sup>, A. Protat<sup>2,\*</sup>**

7 [1]{Université Blaise Pascal, Laboratoire de Météorologie Physique, Aubière, France}

8 [2]{Laboratoire Atmosphère, Milieux et Observations Spatiales, UVSQ, Guyancourt, France}

9 [\*]{now at: Center for Australian Weather and Climate Research, Melbourne, Australia}

10 Correspondence to: E. Fontaine (E.fontaine@opgc.univ-bpclermont.fr)

## 11 12 **Abstract**

13 In this study the density of ice hydrometeors in tropical clouds is derived from a combined  
14 analysis of particle images from 2D-array probes and associated reflectivities measured with a  
15 Doppler cloud radar on the same research aircraft. Usually, the mass-diameter  $m(D)$   
16 relationship is formulated as a power law with two unknown coefficients (pre-factor,  
17 exponent) that need to be constrained from complementary information on hydrometeors,  
18 where absolute ice density measurement methods do not apply. Here, at first an extended  
19 theoretical study of numerous hydrometeor shapes simulated in 3D and arbitrarily projected  
20 on a 2D plan allowed to constrain the exponent  $\beta$  of the  $m(D)$  relationship from the exponent  
21  $\sigma$  of the surface-diameter  $S(D)$  relationship, which is likewise written as a power law. Since  
22  $S(D)$  always can be determined for real data from 2D optical array probes or other particle  
23 imagers, the evolution of the  $m(D)$  exponent can be calculated. After that, the pre-factor  $\alpha$  of  
24  $m(D)$  is constrained from theoretical simulations of the radar reflectivities matching the  
25 measured reflectivities along the aircraft trajectory.

26 The study has been performed as part of the Megha-Tropiques satellite project, where two  
27 types of mesoscale convective systems (MCS) have been investigated: (i) above the African  
28 Continent and (ii) above the Indian Ocean. For the two datasets, two parametrisations are

1 derived to calculate the vertical variability of  $m(D)$  coefficients  $\alpha$  and  $\beta$  as a function of the  
2 temperature. Originally calculated (with T-Matrix) and also subsequently parametrised  $m(D)$   
3 relationships from this study are compared to other methods (from literature) of calculating  
4  $m(D)$  in tropical convection. The significant benefit of using variable  $m(D)$  relations instead  
5 of a single  $m(D)$  relationship is demonstrated from the impact of all these  $m(D)$  relations on  
6 Z-CWC and Z-CWC-T fitted parametrisations.

7

8

## 9 **1 Introduction**

10 The French-Indian satellite Megha-Tropiques (MT), launched in 2011, is primarily devoted to  
11 improve our knowledge about the life cycle of tropical convective systems over ocean and  
12 continents, the environmental conditions for their formation and evolution, their water budget,  
13 and the associated water vapor transport. The most relevant instrument on the MT satellite for  
14 cloud studies is the MADRAS microwave imager having 9 frequencies (18.7 GHz to 157  
15 GHz). Similar satellite missions for tropical cloud studies were TRMM (Tropical Rainfall  
16 Measurement Mission, Huffman et al. 2007; Jensen and Del Genio 2003) or SSM/I (Special  
17 Sensor Microwave/Imager, Spencer et al. 1989). To retrieve the surface rain rate from the  
18 brightness temperatures measured by above satellite missions, retrieval algorithms, as for  
19 example BRAIN (Viltard et al. 2006), are used, which have major sources of uncertainty due  
20 to the variability of the density of ice crystals in the tropical atmosphere.

21 With the overall objective to learn more about the variability of microphysical properties (in  
22 particular density) of ice crystals in tropical convective clouds, two aircraft campaigns  
23 (detailed in section 2) were conducted within the frame of the MT project.

24 The main focus of this study is to characterize the statistical relationship between the mass  
25 and the length (hereafter  $m(D)$ ) of ice crystals by developing a retrieval technique that  
26 combines radar reflectivity and particle imagery, in order to produce reliable calculations of  
27 the condensed water content (CWC) as a function of time and along flight trajectory. This  
28 study focuses on the variability of the  $m(D)$  power law relationship in tropical convective  
29 clouds. Several previous studies have shown significant variability in  $m(D)$  including pre-  
30 factor and exponent of the power law for different flights within one and the same aircraft  
31 campaign (McFarquhar et al. 2007; Heymsfield et al. 2010a, hereafter denoted H10).

1 Concerning the ice crystal growth by pure vapor diffusion it is well known that the crystal  
2 habit is primarily a function of temperature and supersaturation (Bailey and Hallett 2004,  
3 2009; Kobayashi 1993). In addition, collision growth processes (aggregation and riming) in  
4 dynamically more active clouds tremendously complicate the resulting crystal habits and  
5 associated properties (crystal geometry, density, optical properties). Therefore, and to  
6 improve our understanding of microphysical processes in clouds in general, it is necessary to  
7 get a more realistic description of ice crystals and particularly a description of their mass as a  
8 function of their size (Schmitt and Heymsfield 2010; hereafter SH2010).

9 Cloud observations are often related to radar measurements or satellite observations and  
10 associated inversion algorithms. Thus, the forward modeling of the remote sensing signal  
11 (active or passive) and the retrieval of cloud microphysics is linked to the model capacity to  
12 simulate the radiative transfer through a population of ice crystals of complex habits.  
13 Numerous previous studies already related cloud radar reflectivity (usually at a frequency of  
14 94GHz or 35GHz) and in-situ measurements of cloud microphysical properties. For instance,  
15 Protat et al. (2007) and Hogan et al. (2006) calculated the total water content assuming a  
16 constant mass-size relationship for all clouds. Derived Z-CWC relationships often need to be  
17 corrected as a function of temperature. This somewhat translates the lack of knowledge of the  
18 temperature dependency of mass size relationships.

19 The most usual empirical expression used to predict the mass for various types of ice crystal  
20 shapes is formulated as a power law (Locatelli and Hobbs 1974; Mitchell 1996, hereafter  
21 M96; Heymsfield and Westbrook 2010; McFarquhar et al. 2007) which is usually a function  
22 of the maximum length (hereafter  $D_{max}$ ) or the mean diameter (average of the maximum  
23 length in the y axis and the maximum value of x axis; Brown and Francis 1995, hereafter  
24 BF95) of the 2D hydrometeor images.

25 In this paper the mass  $m$  (in gram) is presented as a power law relation of  $D_{max}$  (in  
26 centimeters):

$$27 \quad m(D_{max}) = \alpha \cdot D_{max}^{\beta} \quad (1)$$

28 In other studies the mass (and thus density) of hydrometeors has been determined following  
29 various principles. For example, ice crystals have been collected on a sheet of plastic or a  
30 Petri dish. After taking microphotographs of the crystals, these have been melted to deduce  
31 their mass from the resulting hemispherical drops (Locatelli and Hobbs 1974 ; Mitchell et al.

1 1990). Another method used is to classify hydrometeors according to their crystal habits  
2 associated to specific  $m(D)$  relations for individual habits, following the scheme given by  
3 Magono and Lee (1966). Furthermore, when the CWC mass concentration is measured  
4 directly with simultaneously 2D images of hydrometeors,  $m(D)$  relationships are derived from  
5 integral CWC data and corresponding particle size distributions (hereafter PSD) extracted  
6 from the images. BF95 used simultaneously a Lyman- $\alpha$  absorption hygrometer (Nicholls et al.  
7 1990) and a 2D Optical Array Probe (OAP) to determine coefficients  $\alpha$  and  $\beta$  for cirrus  
8 clouds. Heymsfield et al. (2002) developed an expression of the crystal mass as a function of  
9  $D_{max}$  and the area ratio  $A_r$  (the projected area of an ice particle normalized by the area of a disc  
10 having the same  $D_{max}$ ) for bullet-rosettes present in cirrus clouds. This approach was  
11 confronted with real measurements of CWC measured with a Counterflow Virtual Impactor  
12 (Ogren et al. 1985) and corresponding 2D images (OAP 2DC and 2DP) in cirrus clouds from  
13 airborne measurements. A detailed description of the particle habits which is needed for the  
14 previous approach was provided by the high resolution 2D images from the Cloud Particle  
15 Imager CPI (Lawson et al., 1998). Heymsfield et al. 2002 then used the retrieved  $m(D)$   
16 relationships to compute Ka-band radar equivalent reflectivities, which are in good agreement  
17 with measured reflectivities.

18 Baker and Lawson (2006; hereafter B&L) introduced a new scheme which is a combination  
19 of fundamentals geometric parameters (perimeter, width,  $D_{max}$  and projected area) of the 2D  
20 images to deduce the mass of individual particles. This method was validated against the  
21 dataset of Mitchell et al. (1990) and has the advantage of not requiring particle habit  
22 assumptions.

23 McFarquhar et al. (2007) derived vertical profiles of  $m(D)$  relationships in the stratiform part  
24 of Mesoscale Convective Systems (hereafter MCS) above the North American continent  
25 within and below the melting layer.  $\alpha$  and  $\beta$  coefficients were calculated from measured  
26 reflectivities and PSD deduced from the OAP 2DC and 2DP probes.

27 Schmitt and Heymsfield (2010, hereafter SH2010) have simulated the aggregation of plates or  
28 columns. Therein, fractal 2D and 3D analyses, calculated from the box counting method  
29 (Tang and Marangoni 2006), suggested that the fractal coefficient in the 3D space is equal to  
30  $\beta$ . This allowed deriving a relationship that calculates the exponent  $\beta$  from the 2D fractal  
31 dimension of the 2D images. Once  $\beta$  has been fixed, the pre-factor  $\alpha$  is calculated from the  
32 area measurement with OAP of ice hydrometeors. H10 have calculated  $m(D)$  coefficients by

1 minimizing the differences with measured CWC for different airborne campaigns. They  
2 demonstrate that a strong relationship exists between  $\alpha$  and  $\beta$  coefficients, which was  
3 mathematically demonstrated with a gamma distribution parametrizing the PSD. Furthermore,  
4 they argue that the BF95 relationship overestimates the prefactor  $\alpha$  for stratiform clouds,  
5 whereas  $\alpha$  is underestimated for convective clouds.

6 In our study, bulk CWC measurements were either not performed (MT2010) or of limited  
7 value for MT2011. A deep cone unattended version of the Nevzorov probe has been installed  
8 under the fuselage, showing some enrichment due to ice crystals bouncing from the aircraft  
9 skin. In addition, a relatively high offset led to probe saturation at roughly  $1\text{gm}^{-3}$ .

10 In order to calculate CWC, cloud ice density of hydrometeors needs to be derived from joint  
11 analysis of the radar reflectivity measured by the 94 GHz cloud radar RASTA (Protat et al.  
12 2009), and cloud particle images measured simultaneously with 2D array probes on the same  
13 aircraft. The  $\alpha$  and  $\beta$  coefficients are constrained from particle imagery and from theoretical  
14 simulations of ice crystal images, combined with subsequent simulations of cloud  
15 reflectivities compared to measured ones. In the following section 2 the MT aircraft  
16 campaigns and corresponding in-situ microphysical measurements are described. The  
17 methodology to retrieve  $m(D)$  coefficients for CWC calculations from the variability of the  
18 hydrometeor images and corresponding radar reflectivity measurements is presented in  
19 section 3. Section 4 then presents results on the variability (every 5 seconds during flight) of  
20 calculated  $m(D)$  coefficients. Then the coefficients are parametrized (as a function of  
21 temperature, also mean value) and compared with existing  $m(D)$  relations. All these  $m(D)$   
22 relations are applied to datasets of the two MT flight campaigns, thus calculating CWC, in  
23 order to study their impact on Z-CWC and Z-CWC-T parametrisations fitted to corresponding  
24 measured reflectivity data.

25

## 26 **2 Cloud data from the Megha-Tropiques flight campaigns**

27 Two airborne measurement campaigns have been conducted with the French Falcon 20  
28 research aircraft from SAFIRE (Service des Avions Français Instrumentés pour la Recherche  
29 en Environnement). During the first campaign, The Falcon20 has been flown out from  
30 Niamey (Niger), in August 2010 (hereafter MT2010) during the monsoon season above the  
31 West African continent. The second campaign has been conducted above the Indian Ocean  
32 between November and December 2011 (hereafter MT2011) at Gan (Maldives).

1 While African continental MCS in the monsoon seasons are due to the convergence of wet  
2 colder air masses from the ocean with dry warmer air masses, the convection over the Indian  
3 Ocean is due to the buoyancy of wet air masses leading to weaker convection in our case.  
4 Further studies (Cetrone and Houze 2009; Frey et al. 2011) have discussed differences in the  
5 intensity of tropical convection between pure continental African MCS and more maritime  
6 MCS with some continental influence (for example South Asia for oceanic convection north  
7 of Australia). These studies conclude on deeper convective systems and strongest  
8 precipitation for African MCS as compared to oceanic convection. Then growth processes of  
9 hydrometeors in oceanic convection were to a non negligible extent due to vapor diffusion  
10 producing many dendrites and plates that have been observed. In contrast, for West-African  
11 MCS the hydrometeor growth is more influenced by riming and aggregation processes, thus  
12 leading to observations of abundant ice crystal aggregates and graupel-type particles.

13 A brief description of the research flights and sampled convective cloud systems selected for  
14 this study is presented in Tab. 1. Cloud systems observed during MT2010 were typically  
15 MCS, consisting of a convective and a trailing stratiform part (Houze 2004). Most of the  
16 flights were performed in the stratiform part of these MCS within the temperature range down  
17 to  $-35^{\circ}\text{C}$ . During MT2011, two types of systems were observed: in the first part of the  
18 campaign two MCS systems were sampled, whereas in the second part the convection has  
19 been much less organized and only more isolated smaller systems have been encountered. In  
20 general, flights were performed in the anvil at various constant altitude levels as close as  
21 possible and parallel to the convective line for MT2010. For MT2011 flight pattern were  
22 performed downstream the convective cell, but not crossing the most active part.

23 The Falcon 20 has been equipped with active remote sensing and cloud microphysics in situ  
24 instrumentation. Next to the Doppler Cloud radar RASTA (Protat et al. 2009) in-situ  
25 measurements of microphysical properties were performed using a new generation of Optical  
26 Array Probes (OAP): the 2-D stereo probe (2D-S) from Stratton Park Engineering Company  
27 (SPEC) Inc. which allows to monitor 2D images in the size range  $10\text{-}1280\mu\text{m}$ , and the  
28 Precipitation Imaging Probe (PIP) from droplet Measurement Technologies (DMT) which  
29 measures hydrometeors in the size range of  $100\text{-}6400\mu\text{m}$ .

30 Fig. 1 presents exemplary 2D images of ice crystals observed during the two campaigns. 2D  
31 images are presented as a function of altitude. On the left side of Fig. 1 hydrometeors are  
32 shown that have been observed in continental MCS, whereas on the right side hydrometeors

1 observed in oceanic MCS are presented. In the two first levels (-1°C and -5°C) hydrometeors  
 2 are similar with one exception where at -5°C a dendrite shows up for MT2011. For others  
 3 levels ice crystal shapes are in general different. Besides aggregates, significant amounts of  
 4 individual large pristine ice crystals such as dendrites (typically due to water vapor diffusion  
 5 only) could be observed for MT2011, whereas 2D images for MT2010 generally look more  
 6 like aggregates (more or less rimed) and sometimes graupels.

7 In order to derive particle size distributions and aspect ratios from the 2D images, standard  
 8 corrections of the OAP data have been performed. In particular, rejection of 2D images due to  
 9 shattering (Field et al. 2006, Korolev and Isaac 2005) and also rejection of splashes have been  
 10 applied. Moreover, reconstruction of truncated images which are only partially recorded has  
 11 been applied (Heymsfield and Parrish 1978). Finally, the pixel resolution (10 µm for the 2D-  
 12 S, 100 µm for the PIP) is corrected for the true air speed (Baumgardner and Korolev 1997), in  
 13 order to account for the fixed speed setting during data acquisition.

14 2D images recorded with 2D-S and PIP probes were processed using the software developed  
 15 at LaMP (Laboratoire de Météorologie Physique) for CPI images (Lefèvre 2007) and  
 16 improved for black and white 2D images in order to extract a large variety of geometrical  
 17 parameters, such as maximum diameter  $D_{max}$ , width perpendicular to  $D_{max}$  direction, projected  
 18 area (hereafter  $Sp$ ), and perimeter. Then for each probe, the number particle size distribution  
 19 (PSD) and the mean aspect ratio distribution (hereafter AsD) are calculated as a function of  
 20  $D_{max}$ . With these distributions we build composite distributions for PSD and AsD from both  
 21 probes. The size range of these distributions spans from 50 to 6450 microns in  $D_{max}$ .  
 22 Equations 2 and 3 describe the simple interpolation scheme used to build the composite  
 23 number PSD, an analogue scheme is used to derive AsD composite distributions.

$$\begin{aligned}
 \sum_{D_{max}=50}^{D_{max}<6450} N(D_{max}) \cdot \Delta D_{max} &= \sum_{D_{max}=50}^{D_{max}<450} N_{2DS}(D_{max}) \cdot \Delta D_{max} + C_1(D_{max}) \cdot \sum_{D_{max}=450}^{D_{max}<950} N_{2DS}(D_{max}) \cdot \Delta D_{max} \\
 + C_2(D_{max}) \cdot \sum_{D_{max}=450}^{D_{max}<950} N_{PIP}(D_{max}) \cdot \Delta D_{max} &+ \sum_{D_{max}=950}^{D_{max}<6450} N_{PIP}(D_{max}) \cdot \Delta D_{max}
 \end{aligned} \quad (2)$$

$$\text{with } C_1(D_{max}) + C_2(D_{max}) = 1 ; \text{ and } C_2(D_{max}) = (D_{max} - 450) / (950 - 450) \quad (3)$$

26 These composite distributions are mainly composed of three parts. The first part, which  
 27 comprises the size range of 50-450 microns, is made of pure 2D-S distributions ( $N_{2D-S}$ ),  
 28 whereas the third part between 950-6400 microns is purely taken from PIP ( $N_{PIP}$ )  
 29 distributions. The intermediate second part is obtained by weighting the 2D-S and PIP

1 distributions with a transfer function (equation 3) which increases the weight of the PIP and  
2 decreases the weight of the 2D-S data with increasing  $D_{max}$ . The bin resolution of the  
3 composite distributions is given by  $\Delta D_{max}$  equal to 10 microns. Examples of PSD and AsD are  
4 presented in Fig. 2. Fig. 2a shows the PSD composite distribution and the individual PSDs of  
5 the individual probes. The AsD composite distribution is shown in Fig. 2b. It can be seen that  
6 the transfer function smoothes the transition from the 2D-S to the PIP. In the common size  
7 range [450 $\mu\text{m}$ ; 950 $\mu\text{m}$ ] the two probes 2D-S and PIP are in rather good agreement. The 2D-S  
8 is most reliable and performing well up to particle sizes of 500  $\mu\text{m}$ , beyond the 2D-S starts to  
9 be slowly affected by the truncation of the particles. This is why 2D-S images are taken into  
10 account with decreasing weight in the common size range [450 $\mu\text{m}$ ; 950 $\mu\text{m}$ ]. In contrast, the  
11 PIP is rather reliable beyond 900  $\mu\text{m}$ . Below 900  $\mu\text{m}$ , the PIP particles are taken into account  
12 with increasing weight, in order to ensure the continuity of the composite PSD calculated  
13 from 2D-S and PIP probe images. PSD (also AsD) and RASTA reflectivities are synchronized  
14 and averaged over the same time step of 5 seconds (for better PSD statistics). RASTA  
15 reflectivities measured 300m below (nadir) and 300m above the aircraft (zenith) along the  
16 flight trajectory are linearly interpolated to estimate the radar reflectivity at flight level. The  
17 uncertainty of the radar reflectivity is about 2dBZ, which takes into account measurement  
18 uncertainties and an eventual calibration error. For the MT data set it has been calculated that  
19 the mean reflectivity difference between 300m above and below the plane is in the order of 3  
20 dBZ, which means a reflectivity difference between flight level and 300m above or below of  
21 about 1.5dBZ. This is less than the calibration and measurement error. Furthermore, the  
22 uncertainty in the measured concentrations of hydrometeors is estimated by the probe  
23 suppliers to be 20 %. This uncertainty stems mainly from the calculations of the sampling  
24 volume.

25

### 26 **3 Methodology of $m(D)$ retrieval: Studying 2D and 3D aspects of** 27 **hydrometeors**

#### 28 **3.1 Simulations of artificial ice crystal shapes and associated $S(D)$ and $m(D)$**

29 Optical array probes (OAP) measure the shadow projection of randomly oriented 3D cloud  
30 particles on a 2D plan. Theoretical simulations of 3D crystals have been processed, and are  
31 described in more detail in appendix A. The corresponding 2D projections are based on the



1 principle of randomly oriented 3D particles projected on a 2D plan. These 2D images are  
 2 processed with the same algorithm used for real particle images in order to deduce particle  
 3 projected area  $Sp$  and maximum diameter  $D_{max}$  of each random projection. Overall, 45  
 4 different kind of hydrometeors (or habits) have been simulated and tested. Fig. 3 shows some  
 5 examples of arbitrarily oriented 3D crystals (stellar, columns, plates, capped-columns,  
 6 rosettes, and aggregates of those) that have been projected onto a plan. For each habit type  
 7 numerous simulations and orientations are performed, then the projected surface  $Sp$  is fitted as  
 8 a function of  $D_{max}$  (the relation is denoted  $S(D)$  ; equation 4), and likewise the mass is fitted as  
 9 a function of  $D_{max}$  (see equation 1).

$$10 \quad S(D_{max}) = \gamma \cdot D_{max}^{\sigma} \quad (4)$$

11 We assume random orientation, where each orientation has the same probability, and  
 12 therefore not consider any possible effect of predominant orientation of hydrometeors during  
 13 sampling. Probes are mounted under the wings at a distance of approximatively 0.5m, in  
 14 addition, the probe tips exceed the wing leading edge. Deviations in exponents  $\sigma$  and  $\beta$  are  
 15 further discussed in Appendix A. We assume extreme orientations for different habits, and  
 16 analyse uncertainties of  $S(D)$  and  $m(D)$  relationships due to possible orientation of ice  
 17 crystals.

18 Relationships  $S(D)$  and  $m(D)$  for each type of habit are fitted with power laws (equation 4 and  
 19 equation 1). The resulting exponents  $\sigma$  for  $S(D)$  and  $\beta$  for  $m(D)$  are shown in Fig. 4 and  
 20 reported in Tab. 2. In order to compare with existing values of  $\sigma$  and  $\beta$  found in the literature,  
 21 we have added the values given in M96. In addition, Tab. 2 summarizes the values and the  
 22 associated symbols of each simulated particle habit. The linear relationship fitted for  $\beta$  related  
 23 to  $\sigma$  for 45 simulated habits is presented in equation 5, which is valid for  $\sigma$  in the range [1.05 ;  
 24 2], yielding values for  $\beta$  in the range [1 ; 2.94].

$$25 \quad \beta_{\sigma} (\pm 0.16) = 1.93 \cdot \sigma - 1.02 \quad (5)$$

26 There is no evidence of such a fit, neither in literature, nor in theory. From the obtained  
 27 results one can notice that varying the linear ratio between  $H$  and  $L$  for plates (also valid for  
 28 slender stellars, solid stellars, and rosettes) does not impact significantly  $\sigma$  and  $\beta$ , whereas a  
 29 nonlinear ratio  $H = \sqrt{L}$  has more impact on both exponents. The latter case produces results  
 30 closer to measurements presented by M96 (Tab. 2), with simulations from our study resulting  
 31 in  $\sigma = 1.86$  and  $\beta = 2.49$  and M96 measurements resulting in  $\sigma = 1.85$  (for  $D_{max} < 100\mu m$ ) and  $\beta$

1 = 2.45, respectively. For  $D_{max} > 100 \mu\text{m}$ , results are not readily comparable with the M96  
2 results as in their study random orientation is not assumed. Regarding columns, an increase of  
3 the ratio H/L has more impact on  $\sigma$  and  $\beta$ . As stated for hexagonal plates, also for columns the  
4 nonlinear ratio  $L = \sqrt{H}$  brings the simulations closer to the M96 measurements, with  $\sigma = 1.48$   
5 and  $\beta = 1.78$  for simulations (this study) and  $\sigma = 1.41$  and  $\beta = 1.74$  for the M96  
6 measurements. Other habits from the M96 measurements are not comparable to our  
7 simulations.

8 In view of the results produced by the 3D simulations, it seems that  $\beta$  (and also  $\sigma$ ) does not  
9 relate much to the sphericity of the crystal shape, but more to how a population of ice crystals  
10 is growing in the 3D space (axis x, y, z) as a function of its evolution in direction of its  
11 maximum length. The behavior of  $\beta$  the exponent for plates and stellars but also for rosettes  
12 shows that, if the crystal height grows at the same speed as the length (which is a combination  
13 of the growth on 2 axis), then  $\beta$  is close to 3. In contrast, if the growth in length is two times  
14 larger than the height, then  $\beta$  is closer to 2.5. Finally, if the height remain constant while the  
15 length is growing, then  $\beta$  gets close to 2.

### 16 **3.2 Surface-diameter relationships of natural hydrometeors**

17 This section focuses on the S(D) relationship (see equation 4) and also on the correlation  
18 which exists between  $D_{max}$ ,  $Sp$ , and the mass of hydrometeors. Since ice crystals have  
19 complex and varied shapes, the description of their volume (or mass) and their projected area  
20  $Sp$  as a function of the particle diameter cannot be described unambiguously with constant  $\sigma$   
21 exponents (for S(D)) or  $\beta$  (for m(D)). In this study, S(D) power law relations are calculated  
22 for 5-seconds steps and are synchronized with PSD and RASTA reflectivity. To calculate  
23 S(D), we plot the mean  $Sp$  of the particles versus their  $D_{max}$  (Fig. 5) for the two probes.  $Sp$  are  
24 averaged by bins in order to get S(D) independently of the ice crystals concentration. S(D)  
25 relations then are fitted by a power law described by  $\gamma$  and  $\sigma$ , for both probes, respectively.  
26 On a log-log scale,  $\ln(\gamma)$  represents the y-axis intercept and  $\sigma$  the slope of the linear  
27 relationship such that  $\log(S) = \sigma \cdot \ln(D) + \ln(\gamma)$ . S(D) relationships for the 2D-S and PIP probes  
28 are calculated using particles larger than  $250\mu\text{m}$  and  $950\mu\text{m}$ , respectively. As shown in Fig. 5  
29 S-D relationships calculated for submillimetric (2D-S) and millimetric particles (PIP) can  
30 deviate. One can suppose that when S(D) of 2D-S and PIP are different, this implies to use  $\sigma$   
31 deduced from the 2D-S images ( $\sigma_{2D-S}$ ) to calculate the  $\beta$  exponent for sub millimetric particles

1 ( $\beta_{2D-S}$ ) and  $\sigma$  deduced from the PIP images ( $\sigma_{PIP}$ ) to calculate the  $\beta$  exponent for the super-  
 2 millimetric particles ( $\beta_{PIP}$ ). Then CWC would be calculated as follows:

$$3 \quad CWC = \sum_{D_{max}=55\mu m}^{D_{max}=Dc} N(D_{max}) \cdot \alpha_{2DS} \cdot D_{max}^{\beta_{2DS}} \cdot \Delta D_{max} + \sum_{D_{max}=Dc}^{D_{max}=6450} N(D_{max}) \cdot \alpha_{PIP} \cdot D_{max}^{\beta_{PIP}} \cdot \Delta D_{max} \quad (6).$$

4 Having fixed  $\beta_{2D-S}$  and  $\beta_{PIP}$  would still mean that when constraining the prefactor of the m(D)  
 5 relation one needs to solve one equation with two unknowns for the two probes:  $\alpha_{2D-S}$  and  
 6  $\alpha_{PIP}$ .

7 Therefore, we introduce here a single  $\sigma$  exponent taking into account images from 2D-S and  
 8 PIP probes, in order to calculate the variability of the m(D) coefficients from the variability of  
 9 S(D) relationships.

$$10 \quad \sigma = \frac{\sum_{D_{max}=250\mu m}^{950\mu m} N(D_{max}) \cdot S(D_{max})}{\sum_{D_{max}=250\mu m}^{6450\mu m} N(D_{max}) \cdot S(D_{max})} \cdot \sigma_{2DS} + \frac{\sum_{D_{max}=950\mu m}^{6450\mu m} N(D_{max}) \cdot S(D_{max})}{\sum_{D_{max}=250\mu m}^{6450\mu m} N(D_{max}) \cdot S(D_{max})} \cdot \sigma_{PIP} \quad (7)$$

11 This particular  $\sigma$  of equation 7 is calculated by weighting the exponent  $\sigma$  of each probe ( $\sigma_{2D-S}$ ,  
 12  $\sigma_{PIP}$ ) with the ratio of the surface of ice crystals contained in the size range of the individual  
 13 probe (size range where individual S(D) relationship is calculated) over the entire surface  
 14 within the total size range covered by both probes.

### 15 3.3 Mass-diameter coefficients and CWC retrieval

16 In order to better understand the importance of coefficients  $\alpha$  and  $\beta$  in eq. 1 and their impact  
 17 on the retrieved CWC, reflectivity simulations at 94GHz have been performed and compared  
 18 with corresponding measured reflectivities along the flight trajectory. Simulations of radar  
 19 reflectivities are complex when considering non-spherical ice crystals. Hogan et al. 2011,  
 20 have used the Rayleigh-Gans approximation to simulate the reflectivity of ice hydrometeors  
 21 interpreted as oblate spheroids (at 10GHz and 94GHz). Therein a constant aspect ratio of 0.6  
 22 was assumed to describe the flattening of the spheroids. Applying the BF95 parametrisation to  
 23 calculate CWC, a good agreement has been achieved between simulated and measured  
 24 reflectivities.

25 In this study, backscatter properties of the hydrometeors have been simulated with the T-  
 26 matrix method (Mishchenko et al. 1996) for crystals and/or with Mie theory for spherical

1 particles. In order to model the scattering properties of the ice particles, these particles are  
 2 assumed to be oblate spheroids with a flattening that equals the mean aspect ratio  $\overline{As}$  of the  
 3 hydrometeors with  $D_{max} < 2\text{mm}$ , which impact most the simulated reflectivity:

$$4 \quad \overline{As} = \sum_{D_{max}=55\mu\text{m}}^{2000\mu\text{m}} Pi(D_{max}) \cdot As(D_{max}) \quad (8),$$

5 where the  $Pi(D_{max})$  is the weighting function and is calculated as follows:

$$6 \quad Pi(D_{max}) = \frac{N(D_{max}) \cdot D_{max}^3 \cdot \Delta D_{max}}{\sum_{D_{max}=55\mu\text{m}}^{2000\mu\text{m}} N(D_{max}) \cdot D_{max}^3 \cdot \Delta D_{max}} \quad (9).$$

7  $N(D_{max})$  is the concentration of the hydrometeors and  $As(D_{max})$  their aspect ratio, both  
 8 functions of  $D_{max}$ .  $\overline{As}$  is calculated every 5 seconds as is done for the composite PSD,  $\sigma$ , and  
 9 radar reflectivity. Indeed at 94GHz the hydrometeors with  $D_{max} > 2\text{mm}$  are not invisible, but  
 10 the increase of their backscattering cross section ( $Q_{back}$ ; Fig. 6) as a function of their size is  
 11 not sufficient taking into account the very small crystal concentrations beyond a few  
 12 millimeters. Thus, they do not impact the simulated reflectivity. Fig. 6 also shows the impact  
 13 of  $\overline{As}$  on the effective reflectivity for 94 GHz, for  $\overline{As}$  varying between 0.5 and 1. For  $\overline{As} = 1$   
 14 particles are spherical and therefore the Mie solution of the Maxwell's equation can be used.  
 15 For diameters less than 600-900  $\mu\text{m}$  simulated radar reflectivities agree well with those  
 16 calculated using the Rayleigh approximation. As it can be seen in this figure, the so-called  
 17 'Mie effects' appear only for larger diameters and decreasing aspect ratio  $\overline{As}$ . The  $Pi(D_{max})$   
 18 weighting function impacts the mean aspect ratio  $\overline{As}$  which will be subsequently used to  
 19 constrain the T-matrix simulations of the radar reflectivity. In  $Pi(D_{max})$  the maximum length  
 20 of hydrometeors is taken at its third order, to take into account the impact of the hydrometeors  
 21 in the sampling volume. This choice is a compromise to accomplish for the lack of knowledge  
 22 to constrain the variability of  $Q_{back}$  for natural ice crystals and previous approximations using  
 23 the Mie solution to model  $Q_{back}$ . Instead of the third order of  $D_{max}$ , we could have chosen the  
 24 number concentration  $N(D_{max})$  or  $N(D_{max}) \cdot S(D_{max})$ , both may overestimate the smallest ice  
 25 crystals, while  $D_{max}^6$  (Rayleigh approximation) does not seem to be the best choice either in  
 26 this context.

27 In general, we consider hydrometeors as a homogeneous mixture of ice and/or air. In order to  
 28 identify cases where the mixed phase (ice and water) was present, signals of the Rosemount

1 Ice Detector (RICE) have been analyzed. The RICE probe is in fact a supercooled water  
 2 detector. Few and extremely short cases were identified where the RICE probe showed  
 3 supercooled water. Data containing possible supercooled water have been excluded from  
 4  $m(D)$  calculations for ice.

5 The dielectric properties of ice particles are linked to the mass-diameter relationship  
 6 characterised by the fraction of ice  $f_{ice}$  (equation 10) in the hydrometeors. Equation 10  
 7 explains how the ice fraction of the solid hydrometeors are calculated, with  $\rho_{ice} = 0.917 \text{ g cm}^{-3}$ .  
 8 The ice fraction  $f_{ice}$  cannot exceed 1.

$$9 \quad f_{ice} = \min \left( 1, \frac{\alpha \cdot D_{max}^{\beta}}{\frac{\pi}{6} \cdot \rho_{ice} \cdot D_{max}^3} \right) \quad (10).$$

10 Once  $f_{ice}$  is determined the refractive index is calculated using the approximation of Maxwell  
 11 Garnet (1904). The mass of the spheroid does not depend on the aspect ratio  $\overline{As}$ , but the  
 12 backscattering properties do. By means of the T-matrix method the backscattering coefficient  
 13 of a particle is calculated assuming the particle volume as an oblate spheroid with a diameter  
 14  $D_{T-matrix}$ :

$$15 \quad D_{Tmatrix} = D_{max} \cdot \sqrt[3]{\frac{1}{As}} \quad (11).$$

16 In order to calculate the 94 GHz radar reflectivity, the particle number distribution  $N(D_{max})$ ,  
 17 the mean aspect ratio  $\overline{As}$ , the ice fraction  $f_{ice}$  of the hydrometeors, and the  $\beta$  and  $\alpha$  coefficients  
 18 of the mass-diameter relation (eq. 1) must be known or assumed. Fig. 7 gives an outline of the  
 19 technique developed to retrieve the  $m(D)$  coefficients. After fixing  $\beta_{\sigma}$  from equation 5, then  
 20 the prefactor  $\alpha_{\sigma}$  is determined by minimizing the difference between the simulated and  
 21 measured reflectivities. Then the corresponding  $CWC$  in  $\text{g m}^{-3}$  is calculated from the PSD and  
 22 the mass-diameter coefficients:

$$23 \quad CWC(\alpha_{\sigma}, \beta_{\sigma}) = 10^3 \cdot \sum_{D_{max}=50\mu m}^{D_{max}=6400\mu m} N(D_{max}) \cdot \alpha_{\sigma} D_{max}^{\beta_{\sigma}} \cdot \Delta D_{max} \quad (12).$$

24 Fig. 8 shows the temporal evolution of the PSD, mean aspect ratio  $\overline{As}$ , exponent  $\beta_{\sigma}$ , derived  
 25  $\alpha_{\sigma}$ , and calculated  $CWC(\alpha_{\sigma}, \beta_{\sigma})$  for a cloud sequence of flight 18 during MT2010. The

1 temporal variabilities of the PSD,  $\overline{A_s}$ , the exponent  $\beta_\sigma$ , constrained pre-factor  $\alpha_\sigma$ , and  $CWC$   
 2 are considerable.

3 The uncertainty of this method is evaluated in systematically varying  $\beta$  in the interval [1;3],  
 4 while for each  $\beta$  the pre-factor  $\alpha$  is deduced accordingly by minimizing the difference  
 5 between the simulated and measured reflectivities. Then the corresponding  $CWC$  values are  
 6 calculated. For a given time step of 5 seconds the calculated minimum and maximum values  
 7 of  $CWC$  ( $CWC_{min}$  and  $CWC_{max}$ , respectively) are used to estimate the maximum uncertainty  
 8 ( $\Delta CWC_{max}$ ) of the retrieved  $CWC$ .  $\Delta CWC_{max}$  is defined as the maximum difference between  
 9  $CWC(\alpha_\sigma, \beta_\sigma)$  and the largest or smallest value of  $CWC$ . This maximum uncertainty can be also  
 10 calculated in terms of the relative error in percent:

$$11 \quad 100. \frac{\Delta CWC_{max}}{CWC(\alpha_\sigma, \beta_\sigma)} = 100. \frac{MAX( [|CWC_{min} - CWC(\alpha_\sigma, \beta_\sigma)| ; |CWC_{max} - CWC(\alpha_\sigma, \beta_\sigma)| ] )}{CWC(\alpha_\sigma, \beta_\sigma)} \quad (13).$$

12 For both measurement campaigns MT2010 and MT2011, Fig. 9 shows the distribution of  
 13  $\Delta CWC_{max}$  in percent. For most of the calculated  $CWC$  values the maximum errors remain  
 14 below 30%. Average values of the maximum deviations in  $CWC$  are 26% for MT2010 and  
 15 25% for MT2011, respectively.

16  $CWC(\alpha_\sigma, \beta_\sigma)$  is compared with the B&L scheme computing  $CWC_{B\&L}$  from the 2D images.  
 17 This method was chosen among others because it does not require any assumption on particle  
 18 habit and calculates the condensed mass particle by particle. Fig. 10 shows calculated  
 19  $CWC(\alpha_\sigma, \beta_\sigma)$  versus  $CWC_{B\&L}$ . The two  $CWC$  estimates are fitted using a power law. The  
 20 exponent found is close to 1 which indicates that we are close to linearity between the two  
 21 calculations for the two campaigns: 1.03 for MT2010 (Fig. 10a) and 1.01 for MT2011 (Fig.  
 22 10b). For MT2010  $CWC(\alpha_\sigma, \beta_\sigma)$  is 14% larger than  $CWC_{B\&L}$ , whereas for MT2011  $CWC(\alpha_\sigma,$   
 23  $\beta_\sigma)$  are close to  $CWC_{B\&L}$ . The data set of hydrometeors establishing the above B&L scheme  
 24 stems from winter storms in the central Sierra Nevada in the western part of the North  
 25 american continent. The crystals have been collected at the ground, and subsequently fitted to  
 26 build the B&L scheme. The B&L scheme seems more appropriated to the MT2011 dataset  
 27 than the MT2010 dataset. Comparisons between the two  $CWC$  retrieval methods also exhibit  
 28 good correlation coefficients of 0.89 for MT2010 and 0.91 for MT2011, respectively. In  
 29 addition, error bars for all analyzed  $CWC$  are given in Fig. 10 representing their minimum  
 30 and maximum values which were determined using equation 13.

### 3.4 Impact of measurement uncertainties on $m(D)$ and CWC retrieval

This section quantifies the impact of the measurement uncertainties in radar reflectivity,  $\overline{As}$ ,  $\beta$ , PSD and also the probe shattering effect on the calculation of  $\alpha$  and CWC. In order to quantify the impact of various measurement errors, the retrieval of  $\alpha$  and subsequent calculation of CWC were performed in shifting measured values by the amount of the respective measurement error.

First, if reflectivity measured with the radar RASTA is shifted by +2 dBZ, then CWC increases by about 21% (Table 3). Second, if the mean aspect ratio  $\overline{As}$  increases by 20% (due to a different calculation of the weighting function  $Pi$ , for example as a function of  $N(D_{max})$ ), then CWC increases by about 12% (Table 4). Likewise, if  $Pi(D_{max})$  is calculated from  $N(D_{max}) \cdot S(D_{max})$ , then  $\overline{As}$  increases by about 10% and CWC by about 6%. Third, a decrease in  $\beta_\sigma$  of -0.16, leads to a decrease in  $\alpha_\sigma$  of about 28% on average, whereas an increase in  $\beta_\sigma$  of +0.16 increases the value of  $\alpha_\sigma$  by about 42% on average. Fourth, in order to quantify the impact of particle shattering,  $\alpha$  and CWC were calculated once without applying the removal algorithm. In this case the  $S(D_{max})$  relationship is little impacted on average and the exponent  $\beta_\sigma$  of  $m(D_{max})$  increases slightly by approximately +0.5%. The retrieved prefactor  $\alpha_\sigma$  is impacted by about +4% and CWC increases by about +5%.

With respect to the concentration uncertainty  $\Delta N$  when assuming an uncertainty in sampling volume of roughly 20% (uncertainty equally distributed over all sizes) we can estimate an uncertainty of 20% in  $\alpha_\sigma$ . While the reflectivity is not impacted by the measurement uncertainty on the PSD, the CWC which corresponds to this reflectivity is not impacted to. Then, the CWC calculation from two concentrations  $N_1$  and  $N_2$  which gives the same CWC can be expressed as it follows:

$$CWC = \int_0^{\infty} N_1(D) \cdot \alpha_1 \cdot D^\beta \cdot dD = \int_0^{\infty} N_2(D) \cdot \alpha_2 \cdot D^\beta \cdot dD \quad (14)$$

Furthermore, assuming that  $\beta$  here is not impacted because the concentration uncertainty is assumed to be equally distributed over all diameters, then with  $N_1(D) = (1 \pm \frac{\Delta N}{N}) \cdot N_2(D)$  we can derive  $\alpha_1 = (1 \mp \frac{\Delta N}{N}) \cdot \alpha_2$ , from where we conclude on an uncertainty for  $\alpha_\sigma$  and CWC of roughly 20%. The concentration uncertainties associated to the shattering are nevertheless

1 mainly impacting the smaller sizes, the uncertainty of  $\alpha_\sigma$  and CWC is then considered  
2 significantly smaller.

3

#### 4 **4 m(D) relationship and impact on Z-CWC calculation**

##### 5 **4.1 m(D) variability**

6 In the previous section, it has been demonstrated how  $\beta_\sigma$  is derived from  $S(D_{\max})$  power laws  
7 that are fitted separately for 2D-S and PIP image data with final calculation of one single  
8 exponent  $\sigma$ , yielding then  $\beta_\sigma$  based on the theoretical work presented in section 3.1. Then  $\alpha_\sigma$  is  
9 constrained by reflectivities of RASTA, including subsequent calculation of CWC.

10 The two m(D) coefficients ( $\alpha_\sigma, \beta_\sigma$ ) appear to be strongly correlated with each other, with a  
11 correlation coefficient (cc) that equals 0.81 for MT2010 (Fig. 11a) and 0.92 for MT2011 (Fig.  
12 11b). This result was observed and discussed in H10. In H10, m(D) coefficients were found  
13 by minimizing the differences between CWC estimated from particle imagery and measured  
14 bulk CWC. This was performed flight-by-flight for different airborne campaigns. Their  
15 dataset was divided into two types of cirrus: convective cirrus and stratiform cirrus. H10  
16 obtained trends for each type of cirrus by fitting the mean of the prefactor (here  $\alpha$ ) as a  
17 function of the exponent (here  $\beta$ ). In Fig. 11, the power law fit obtained for convective cirrus  
18 by H10 is added as a black line. We note in the semi-log representations of Fig. 11, that the  
19 slope derived by H10 is exceeding the slopes calculated for MT2010 and MT2011,  
20 respectively. This may be explained by the fact that  $\beta$  coefficients in H10 have been  
21 calculated differently as compared to this study. However, both studies show that  $\alpha$  (hereafter  
22  $\alpha_\beta$ ) can be fitted as an exponential function of  $\beta$  (equations 15 and 16 for MT2010 and  
23 MT2011, respectively).

$$24 \quad MT2010: \quad \alpha_\beta = 7.10^{-5} \cdot e^{2.11 \cdot \beta_\sigma} \quad (15)$$

$$25 \quad MT2011: \quad \alpha_\beta = 2.10^{-5} \cdot e^{2.65 \beta_\sigma} \quad (16)$$

26 Furthermore, Fig. 11 reveals that temperature has an impact on the relationship between  $\alpha_\sigma$   
27 and  $\beta_\sigma$ , which was not discussed in H10. In particular, for a given exponent  $\beta_\sigma$ , the prefactor  
28  $\alpha_\sigma$  increases with temperature. Equations 17 and 18 take into account the temperature



1 dependency of the  $\alpha$ - $\beta$  relation, where the temperature is given in K and the resulting  
 2 prefactor is denoted  $\alpha_{\beta,T}$ .

$$3 \quad MT2010: \quad \alpha_{\beta,T} = 7.10^{-5} \cdot e^{2.11\beta\sigma} \cdot (0.05888 \cdot e^{0.0107T} + 6.4 \cdot 10^{-17} \cdot e^{0.133T}) \quad (17),$$

$$4 \quad MT2011: \quad \alpha_{\beta,T} = 2.10^{-5} \cdot e^{2.65\beta\sigma} \cdot 0.011834 \cdot e^{0.01535T} \quad (18).$$

5 Table 5 shows ratios of  $\alpha_{\beta}$  and  $\alpha_{\beta,T}$  (calculated according to equations 15, 16, 17, and 18) over  
 6  $\alpha_{\sigma}$  (constrained by T-matrix simulations). Average and median values of these ratios are  
 7 particularly close to 1. The first and third quartiles illustrate the narrowing around the median  
 8 ratio when parametrizing the  $\alpha$  as a function of  $\beta$  and the temperature for the two campaigns.

9 For the two MT campaigns the following mean coefficients of  $m(D)$  have been deduced:

$$10 \quad MT2010: \quad m(D_{\max}) = 0.0090 \cdot D_{\max}^{2.23} \quad (19),$$

$$11 \quad MT2011: \quad m(D_{\max}) = 0.0054 \cdot D_{\max}^{2.05} \quad (20).$$

12 In Fig. 12 these relationships are compared against  $m(D)$  deduced in H10 on the hand for the  
 13 NAMMA (NASA African Monsoon Multidisciplinary Analyses; Zipser et al. 2009) campaign  
 14 and on the other hand for clouds which were convectively generated (hereafter cv-gt) during  
 15 CRYSTAL-FACE (Cirrus Regional Study of Tropical Anvils and Cirrus Layers–Florida Area  
 16 Cirrus Experiment ; Jensen et al. 2004) and TC4 (Tropical Composition, Cloud and Climate  
 17 Coupling ; Toon et al. 2010; Heymsfield et al. 2010b). NAMMA was performed above the  
 18 African continent. CRYSTAL-FACE took place in the southern part of Florida, whereas TC4  
 19 includes convective systems close to the Inter-Tropical Convergence Zone (ITCZ) and other  
 20 strong convection developed along the coast of Costa Rica. H10 fixed  $m(D)$  coefficients for  
 21 NAMMA such that  $\alpha = 0.011$  and  $\beta = 2.1$  and for cv-gt (CRYSTAL-FACE+TC4)  $\alpha=0.0063$   
 22 and  $\beta=2.1$ . Furthermore,  $m(D)$  findings from M96 are also included in that figure.  $m(D)$   
 23 relations of MT2011 and H10 for clouds convetively generated are very similar. The mean  
 24  $m(D)$  derived for MT2010 yields crystal masses that are a factor of two smaller than those  
 25 given by H10 for NAMMA. Still, mean  $m(D)$  derived for MT2010, MT2011 and H10(cv-gt)  
 26 reveal higher masses than those given by M96 (for different crystal species) with the  
 27 exception for the lump graupel. The fact that H10 (NAMMA) found largest mass for ice  
 28 hydrometeors below 1mm in size may suppose that ice crystals were more rimed particles in  
 29 the vicinity of the convective part of MCS (NAMMA campaign) as compared to their  
 30 stratiform part (MT2010).

1 Fig. 13 presents trends of m(D) coefficients  $\alpha_\sigma$  and  $\beta_\sigma$  with cloud altitude in terms of  
 2 temperature. The variability of m(D) coefficient at a given temperature is important. Average  
 3 m(D) coefficients (large stars in figure 13) have been calculated for temperature intervals of 5  
 4 K (in Fig. 13 large stars represent median values for respective 5K temperature intervals). The  
 5 calculated profiles for MT2011 data include solely flights 45 and 46 with a well developed  
 6 stratiform region of an extended convective system. Mean values of  $\alpha_\sigma$  and  $\beta_\sigma$  are not  
 7 calculated beyond 272.5K temperature level, since the T-Matrix retrieval method does not  
 8 take into account the liquid water at the surface of melting ice crystals. This should have an  
 9 effect of increased reflectivity of ice crystals, leading to an underestimation of m(D)  
 10 coefficients. On average, mean  $\beta_\sigma$  coefficients (Fig. 13a) are larger for MT2010 than for  
 11 MT2011, whereas mean  $\alpha_\sigma$  coefficients (Fig. 13b) are more similar and in the same order  
 12 between the level 260K-245K. The mean profiles show a decrease of mean  $\alpha_\sigma$  and  $\beta_\sigma$   
 13 coefficients with decreasing temperature described by equations 21 and 22:

$$14 \quad MT2010: \quad \begin{cases} \ln(\alpha_T) = 0.0020 \cdot e^{0.0037T} + 5.10^{-17} \cdot e^{0.1213T} \\ \beta_T = 7.13 \cdot e^{-0.0053T} + 5.4 \cdot 10^{-7} \cdot e^{0.0435T} \end{cases} \quad (21)$$

$$15 \quad MT2011: \quad \begin{cases} \ln(\alpha_T) = 1.98 \cdot 10^{-6} \cdot e^{0.0310T} \\ \beta_T = 1.81 \cdot e^{-0.000755T} - 1.027 \cdot 10^7 \cdot e^{-0.07454T} \end{cases} \quad (22)$$

16 In addition,  $\alpha$  and  $\beta$  profiles given by SH2010 for CRYSTAL-FACE and ARM (Atmospheric  
 17 Radiation Measurement) campaigns are added to figure 13. This latter dataset includes  
 18 midlatitude cirrus clouds generated from large scale uplift above the North American  
 19 continent. Globally,  $\beta_\sigma$  of MT2010 are similar to  $\beta$  of CRYSTAL-FACE, and  $\beta_\sigma$  of MT2011  
 20 are similar to  $\beta$  of ARM given in SH2010.

21 Table 6 shows ratios of  $\alpha_T$  over  $\alpha_\sigma$  and  $CWC(\alpha_T, \beta_T)$  over  $CWC(\alpha_\sigma, \beta_\sigma)$ , as well as differences  
 22 between  $\beta_T$  and  $\beta_\sigma$ . In general,  $\alpha_\sigma$  for MT 2010 and MT2011 are overestimated by the fitted  $\alpha_T$ ,  
 23 whereas  $\beta_\sigma$  is underestimated for MT2010 and overestimated for MT2011 by the fitted  $\beta_T$ .  
 24 Finally, the resulting  $CWC$  calculations lead to average ratios of  $CWC(\alpha_T, \beta_T)/CWC(\alpha_\sigma, \beta_\sigma)$   
 25  $\approx 1.03$  (median value  $\approx 1.01$ ) for MT2010 and  $CWC(\alpha_T, \beta_T)/CWC(\alpha_\sigma, \beta_\sigma) \approx 0.94$  (median value  
 26  $\approx 0.90$ ) for MT2011.

27

## 1 4.2 m(D) impact on Z-CWC and Z-CWC-T

2 In the past, numerous studies have been dedicated to relating CWC to radar reflectivity (Liu  
3 and Illingworth 2000; Hogan et al. 2006; Protat et al. 2007). These studies illustrate that CWC  
4 can be estimated from the radar reflectivity at 94GHz or 35GHz using solely Z-CWC  
5 relationships, but also when adding a temperature dependency (Z-CWC-T relationship). In the  
6 following,  $CWC(\alpha, \beta)$  has been calculated for MT2010 and MT2011 datasets according to 7  
7 different methods: (1) T-matrix ( $CWC(\alpha_\sigma, \beta_\sigma)$ ), (2) equations 17-18 ( $CWC(\alpha_{\beta,T}, \beta_\sigma)$ ), (3)  
8 equations 21-22 ( $CWC(\alpha_T, \beta_T)$ ), (4) mean coefficients of equations 19-20 ( $CWC(\alpha=0.0090,$   
9  $\beta=2.23$  for MT2010) and  $CWC(\alpha=0.0054, \beta=2.05$  for MT2010)), (5) BF95 parametrisation,  
10 (6) and (7) from H10 for NAMMA and cv-gt parametrisations, respectively. In order to use  
11 the BF95 m(D) relationship, PSD were calculated for both MT campaigns such that the  
12 particle diameter is  $D = (Lx+Ly)/2$ . H10 (NAMMA) parametrisation is used solely for the  
13 MT2010 PSD data, whereas H10 (cv-gt) parametrisation is used for the MT2011 PSD data.  
14 Table 7 gives an overview of Z-CWC and Z-CWC-T fitted relationships between different  
15  $CWC(\alpha, \beta)$  calculated with above methods and measured radar reflectivities (RASTA). The  
16 fitted Z-CWC relations are presented in Fig. 14, whereas fitted Z-CWC-T relations are  
17 presented in Fig. 15, with  $Z$  given in  $\text{mm}^6 \text{m}^{-3}$ ,  $CWC$  in  $\text{g m}^{-3}$ , and  $T$  in K. In Fig. 14 and 15,  $Z$   
18 is expressed in dBZ for convenience. Two further relationships given by Protat and al. (2007),  
19 hereafter denoted P2007 are added in Fig 14. Relationships given by P2007 are based on  
20 cloud in-situ observations using a tropical dataset (equation 23a) and from a global dataset  
21 (equation 23b) which includes also mid-latitude and tropical clouds. Note that the BF95 m(D)  
22 relationship has been assumed for all clouds in P2007 calculations.

23  $CWC(Z) = 0.149Z^{0.681}$  Global P2007 (23a)

24  $CWC(Z) = 0.198Z^{0.701}$  Tropics P2007 (23b)

25 Applying P2007 parameterizations for calculating CWC results in significantly larger CWC  
26 values, as compared to estimated CWC of this study for the Megha-Tropiques dataset, which  
27 is particularly true for small reflectivities and most pronounced for MT2011 oceanic  
28 convection. This might be due to the fact that the in-situ database used in P2007 encompasses  
29 a much larger variety of ice clouds, including low CWC cirrus clouds.

30 For MT2010, largest CWC are found when CWC are calculated with the H10 parametrisation  
31 for the NAMMA data. BF95 parametrisation calculates relatively low CWC values for all

1 reflectivities which is also the case for CWC calculated with the T-matrix method for  
2 reflectivities below 0dBZ. The other parametrisations from this study and the P2007  
3 parametrisation for the global dataset are similar and also close to T-matrix calculated CWC  
4 in the range 5dBZ to 15 dBZ.

5 For MT2011, lowest CWC are calculated again with the BF95 parametrisation. CWC  
6 calculations with H10 parametrisation for convectively generated clouds and most of the  
7 parametrisations from this study are rather similar.

8 In general, for both campaigns CWC increases more significantly with the reflectivity when  
9 calculated with the T-matrix method, as compared to CWC calculations from most m(D)  
10 parametrisations (this study, H10, BF95).

11 In principal, Z-CWC-T relationships allow improving the calculation of more realistic CWC  
12 as compared to simpler Z-CWC relationships. In table 8, for the two subsets of fitted  
13 relationships ( $CWC(Z)$  and  $CWC(Z, T)$ ), correlation coefficients (cc) are calculated between  
14  $CWC(\alpha, \beta)$  and  $CWC(Z)$  or  $CWC(Z, T)$  fitted parametrisations, respectively. In addition, an  
15 error calculation (equation 24) is performed with  $error_Z$  and  $error_{Z,T}$  defined as:

16 
$$error_Z = 100 \cdot \frac{|CWC(Z) - CWC(\alpha, \beta)|}{CWC(\alpha, \beta)} \quad \text{or} \quad error_{Z,T} = 100 \cdot \frac{|CWC(Z,T) - CWC(\alpha, \beta)|}{CWC(\alpha, \beta)} \quad (24).$$

17 Table 8 presents expected values (E), median values, first quartiles, third quartiles, and the  
18 90<sup>th</sup> percentiles for  $error_{Z,T}$  and  $error_Z$ , respectively. The lower part of this table presents the  
19 calculation of  $error_{Z,T} - error_Z$  to demonstrate how CWC calculation from reflectivities is  
20 improved when the temperature is parameterized in the fitted relationships between Z and  
21  $CWC(\alpha, \beta)$ .

22 Since the m(D) coefficients within this study have been constrained by the RASTA radar  
23 reflectivity, it is not surprising that  $error_Z$ ,  $error_{Z,T}$ , and also the difference between these two  
24 errors ( $error_{Z,T} - error_Z$ ) are comparably small for CWC derived from T-Matrix method.

25 The fitted CWC-Z relationships for the other methods all produce significantly larger values  
26 for  $error_Z$  with maximum average  $error_Z$  found for methods when  $CWC(\alpha, \beta)$  has been  
27 calculated from constant m(D) coefficients. Furthermore,  $error_Z$  for all methods is generally  
28 larger for MT2011 than for MT2010 dataset. When fitting CWC-Z-T, this does not improve  
29 significantly correlations as compared to CWC-Z fitted relations, neither for the time resolved  
30 T-matrix method nor for  $CWC(\alpha_T, \beta, \beta_\sigma)$  (equations 17 and 18) nor for  $CWC(\alpha_T, \beta_T)$  (equations

21 and 22) methods, since therein the temperature has been implicitly taken into account for  $CWC(\alpha, \beta)$  calculation. In contrast, for the other methods applied to MT2010 and/or MT2011 datasets, as there are mean T-matrix, H10 (NAMMA), H10 (cv-gt), and BF95 the improvement is significant when the temperature is taken into account. Moreover the improvement is more efficient for these other methods for the MT2010 dataset ( $error_Z - error_{Z,T}$  improvement  $> 10\%$ ) as compared to the MT2011 dataset ( $error_Z - error_{Z,T}$  improvement  $\leq 10\%$ ).

Without considering here the original T-Matrix method to calculate CWC, it can be clearly seen from table 8 that the average  $error_{Z,T}$  ( $error_Z$ , respectively) of all 6 remaining methods is smaller for MT2010  $\approx 38\%$  (40%) than for MT2011  $\approx 63\%$  (71%).

The differences in the performance of m(D) parametrisations and respective impact on  $CWC(Z)$  and  $CWC(Z,T)$  relationships for MT2010 and MT2011 can be explained by the fact that the mean aspect ratio  $\overline{As}$  (Fig. 16) for MT2010 cloud particles shows rather constant values with altitude including small standard deviations (Fig. 16a) and even a very small standard deviation around the global average value (Fig. 16b). For MT2011  $\overline{As}$  shows a broader distribution around the global average value and larger standard deviations with altitude (Fig. 16c, 16a). On average  $\overline{As}$  increases with altitude for MT2011, whereas  $\overline{As}$  for MT2010 remains more constant with altitude. Over 80% of the time  $\overline{As}$  for MT2010 is in the range [0.55; 0.65] (Fig. 16b), whereas the broad  $\overline{As}$  spectrum for MT2011 tends to larger values (up to 0.8), as compared to MT2010, which means that MT2011 contains significant amounts of particles with a more spherical aspect ratio.

22

## 23 **5 Discussion and Conclusion**

24 This study presents a method to calculate CWC from particle imagery and radar reflectivity at  
25 94GHz. Cloud particles are represented by oblate spheroids used for reflectivity calculations  
26 with the T-matrix method. The flattening of the spheroid is constrained by the average aspect  
27 ratio  $\overline{As}$  of the 2D images recorded by the 2D-S and the PIP probes. An estimation of the  $\beta$   
28 exponent of the m(D) relationship is derived from the measurements of the projected surface  
29 of 2D images from 2D-S and PIP optical array probes. Then the prefactor  $\alpha$  is calculated from  
30 simulated radar reflectivities matching the corresponding measured reflectivities at 94GHz.  
31 The method has been applied to two different datasets basically sampled in tropical stratiform

1 anvils, the first one sampled over the African Continent (MT2010) and the second one  
2 collected over the Indian Ocean (MT2011).

3 An important variability of the  $m(D)$  coefficients has been found, especially for the MT2011  
4 campaign. This result illustrates the main inconvenience to use a single  $m(D)$  relationships in  
5 tropical clouds. In this study two different parametrisations have been fitted to all constrained  
6  $m(D)$  coefficients (5s time resolution) for continental (MT2010) and oceanic (MT2011)  
7 datasets in tropical convection. The first parametrisation allows us to calculate the  $m(D)$   
8 prefactor as a function of the temperature and the  $m(D)$  exponent, showing that for a given  
9 exponent the prefactor increases with temperature for both campaigns. The second  
10 parametrisation allows us to deduce both  $m(D)$  coefficients (prefactor and exponent) as a  
11 function of the temperature. The latter result is in agreement with results shown in SH2010  
12 for two different dataset of convective clouds in tropical and midlatitude conditions.

13 Furthermore, this study demonstrates how Z-CWC and Z-CWC-T relationships are impacted  
14 by different methods used to retrieve CWC from the measured PSD during MT2010 and  
15 MT2011. In general, the use of a single temperature independent  $m(D)$  relationship for all  
16 clouds is not appropriate, because it excludes the large natural variability of  $m(D)$  (as was also  
17 highlighted in Protat and Williams 2011).

18 For a series of different methods calculating  $CWC(\alpha, \beta)$  (T-Matrix calculation and three  
19 parametrisations presented in this study and also taken from literature such as H10 and BF95)  
20 Z-CWC and Z-CWC-T relationships have been derived between  $CWC(\alpha, \beta)$  and measured  
21 radar reflectivities for MT2010 and MT2011 datasets. Subsequently,  $CWC$  derived from Z-  
22 CWC and Z-CWC-T relations have been confronted with  $CWC(\alpha, \beta)$  originally calculated  
23 with the corresponding method.

24 The main result is shown with the improvement of decreasing error comparing Z-CWC-T  
25 ( $error_{Z,T}$ ) with Z-CWC fitted parametrisations ( $error_Z$ ). For  $CWC(\alpha, \beta)$  methods using  
26 constant  $m(D)$  coefficients (mean T-Matrix, H10(NAMMA), H10(cv-gt), BF95) the error  
27 improvement ( $error_{Z,T} - error_Z$ ) is significant, with on average -12% for MT2010 and -9% for  
28 MT2011 datasets. In contrast, for  $CWC(\alpha, \beta)$  methods which take into account the variability  
29 of  $m(D)$  coefficients ( $CWC(\alpha, \beta)$  as a function of temperature and more precisely as a function  
30 of 2D images in original T-Matrix) the error improvement on average is merely -2% for  
31 MT2010 and -4% for MT2011.

1 The fact that errors from Z-CWC-T (or Z-CWC) relations are larger for MT2011 than for  
2 MT2010 dataset can be explained by the strong variability of the mean aspect ratio  $\overline{As}$  of  
3 cloud particles observed during MT2011, whereas cloud particles for MT2010 are showing a  
4 narrower distribution of  $\overline{As}$ , meaning that crystals aspect ratios have been more uniform.

5 For MT2010 the parametrisation of  $m(D)$  coefficients with temperature (or altitude) seems to  
6 perform well in order to describe the  $m(D)$  coefficients with on average  $CWC(\alpha_T, \beta_T)/CWC(\alpha_\sigma, \beta_\sigma) \approx 1.03$   
7 and  $CWC(\alpha_{\beta,T}, \beta_\sigma)/CWC(\alpha_\sigma, \beta_\sigma) \approx 1.08$ . Likewise, values for MT2011 are  
8  $CWC(\alpha_T, \beta_T)/CWC(\alpha_\sigma, \beta_\sigma) \approx 0.94$  and  $CWC(\alpha_{\beta,T}, \beta_\sigma)/CWC(\alpha_\sigma, \beta_\sigma) \approx 0.99$  respectively. Despite  
9 a good consistency for the both campaigns, the significant variability for example of  $\alpha_T/\alpha_\sigma$ ,  $\beta_T/\beta_\sigma$ ,  
10 and  $CWC(\alpha_T, \beta_T)/CWC(\alpha_\sigma, \beta_\sigma)$  has to be mentioned. The variability can be illustrated by 1<sup>st</sup>  
11 and 3<sup>rd</sup> quartiles and is significantly higher for MT2011 than MT2010. This is due to the fact  
12 that MT2011 dataset covers more variable microphysical properties and/or processes of  
13 hydrometeors (significant contribution of water vapor diffusional growth) compared to  
14 MT2010 and even temperature corrected parametrisations would need to be further refined.

15 An explanation could be that during MT2010 over the African continent the Falcon 20  
16 research aircraft has been flying in stratiform parts of the MCS and despite the attempt to get  
17 close to the convective cells, those have been too vigorous to be entered. Therefore the  
18 microphysical properties of ice crystals in MCS systems sampled during MT2010 have been  
19 relatively similar. In contrast, during MT2011 the less vigorous oceanic convection may have  
20 been sampled partly during an earlier stage of convective activity and also crystal growth  
21 regimes may have been different, leading to an increased variety of microphysical properties.

22

## 23 **APPENDIX A: Description of 3D simulations**

24 Simulations of 3D particle habits have been performed with the overall objective to study the  
25  $S(D)$  and  $m(D)$  relations including correlations between the two exponents of the power laws.  
26 The simulated shapes aim to be realistic or at least comparable to the variety of hydrometeors  
27 found in natural clouds. All crystal shapes considered have 3D characteristics with known  
28 volume or mass and crystal orientations in the 3D space are fairly distributed. Zikmunda and  
29 Vali 1972 show that rimed columns tends to be oriented in a way that the maximum length is  
30 perpendicular to the fall velocity and rimed plates are oriented such that the maximum surface  
31 is perpendicular to the motion. To quantify the uncertainty related to a possible predominant  
32 crystal orientation during sampling, the crystal mass is calculated on the one hand from a

1 minimum  $D_{max}$  (which will be an underestimation with respect to its real value) and on the  
2 other hand from a maximum  $D_{max}$  (Fig. A1). By modeling both types of projected  $D_{max}$   
3 according to the crystal mass and doing this for all simulated shapes, we obtain the maximum  
4 uncertainty related to the projection of possibly oriented 3D hydrometeors projected on a 2D  
5 plane. On average it is found for all simulated habits that  $\Delta\sigma = \pm 0.15$  and  $\Delta\beta = \pm 0.31$ .

6

## 7 **Plates**

8 The schematic of a plate type crystal is presented in Fig. A2. The geometric parameters used  
9 are the thickness  $H$  and the height  $L$  between 2 opposed corners of the hexagon. The  
10 simulations distinguish four types of plates, in order to explore the influence of the ratio  
11 between  $H$  and  $L$  on the fitted power laws. Two simulations have a ratio of  $H/L$  equal to 0.1  
12 and 0.2, whereas in the third simulation  $H$  is equal to the square root of  $L$  and in the fourth  $H$   
13 is constant and equal to 4 pixels. In all these simulations,  $L$  is chosen randomly out of the  
14 interval from 20 to 200 pixels with 1000 thousands simulations of plates in each of the four  
15 cases.

## 16 **Columns**

17 Fig. A3, shows the principal schematic of a column with geometric parameters of height  $H$   
18 and thickness  $L$  between 2 corners of the hexagon. As has been performed for the plates, four  
19 sets of simulations were performed for columns: two with a linear ratio between  $H$  and  $L$ ,  
20 with  $H/L$  equal to 10 and 5, whereas in the third simulation  $L$  is equal to the square root of  $H$   
21 and in the fourth  $L$  is constant and equal to 16 pixels.  $H$  has been chosen out of the size range  
22 of [10;100] pixels with 1000 simulations for columns in each of the four cases.

## 23 **Slender Stellars and more solid stellars**

24 Two types of stellar crystals were simulated with a significant difference in the width of their  
25 branches (Fig. A4). We call these two types slender stellars (lower picture) and solid stellars  
26 (upper picture). For both types of stellars, four sets of 1000 simulations were performed. Two  
27 simulations have a ratio of  $H/L$  equal to 0.1 and 0.2, whereas in the third simulation  $H$  is equal  
28 to the square root of  $L$  and in the fourth simulation  $H$  is constant and equal to 4 pixels.

## 29 **Capped Columns**



1 One type of capped columns was simulated and processed, where the column is capped by  
2 two plates. The schematic description of a capped column is shown in Fig. A5.  $L_1$  is the  
3 height of the two plates (and large stellars) at the top of the column,  $L_2 (=2.5L_1)$  is the  
4 thickness of the column, and  $H (=L_1)$  is its height. For the two simulations  $L_1$  varied between  
5 10 and 100 pixels and the width of the plates (or stellars) has been set to 4 pixels. In total  
6 1000 simulations of capped columns were performed.

## 7 **Rosettes**

8 A rosette with six branches randomly oriented is shown in Fig. A6. To simplify the scheme of  
9 the bullets that constitute the rosette, the bullets are assimilated as hexagonal columns. All the  
10 bullets belonging to the same rosette have identical size parameters, where  $H$  is the bullet's  
11 height,  $L$  its thickness, and  $N$  the maximum number of bullets building the rosette.

12 In total, eight series of simulations were performed, varying  $N$  between 3 and 6 bullets. Two  
13 simulation series have been performed with  $N$  equal to 3 and where the bullets are described  
14 either by  $L$  equal to the square root of  $H$  or  $L$  equal to 5 pixels.  $H$  has been chosen out of the  
15 size range of 5 to 50 pixels.

16 Two sets of simulations followed where  $N$  is equal to 4 and where the bullets are described by  
17  $L$  equal to the square root of  $H$  or  $L$  equal to 10 pixels.  $H$  has been chosen out of the size  
18 range of 10 to 100 pixels.

19 One set of simulations was performed where  $N$  is equal to 5 and where the bullets are  
20 described by the ratio  $L/H$  equal to 0.5.  $H$  has been chosen out of the size range of 10 to 100  
21 pixels.

22 Finally, three additional sets of simulations were performed where  $N$  is equal to 6 and where  
23 the bullets are described either by  $L$  equal to the square root of  $H$  or by  $L$  equal to 10 pixels or  
24 where the ratio  $L/H$  equal to 0.25.  $H$  has been chosen out of the size range of 10 to 100 pixels.  
25 All series were studied with 1000 simulations of rosettes.

## 26 **Aggregates of individual crystal shapes**

27 Furthermore, aggregates of the individual shapes presented above were also simulated.  
28 Without going into some details of crystal aggregation processes (Westbrook et al. 2004),  
29 here we solely study the phenomenon of 3D ice crystal aggregates projected on a 2D plane.  
30 The number of individual crystals ( $N_{agg}$ ) used to form an aggregate has been varied.  
31 Individual crystals are randomly oriented in the 3D space, before they stick together forming

1 the aggregate. An example of an aggregate of spheres is shown in Fig. A7.  $N$  is the random  
 2 number of spheres, ranging between 3 and 50, which are aggregated, and  $D$  is the diameter of  
 3 one sphere which is set constant and equals 6 pixels. In total 1000 simulations of aggregated  
 4 spheres were performed.

5  
 6

## 7 **APPENDIX B: List of Symbols**

8	2D-S	2D stereographic optical array probe with a resolution of $10\mu\text{m bin}^{-1}$
9	2D-C	2D cloud particle optical array probe with a resolution of $25\mu\text{m bin}^{-1}$
10	2D-P	2D precipitation particle optical array probe with a resolution of $200\mu\text{m bin}^{-1}$
11	$\alpha$	pre-factor of mass-diameter relationship in general
12	$\alpha_\beta$	pre-factor of mass-diameter relationship calculated from the T-matrix method
13		when $\beta$ is calculated from equation 5
14	$\alpha_T$	pre-factor of mass-diameter relationship calculated as a function of the
15		temperature (equations 21 and 22)
16	$\alpha_{\beta,T}$	pre-factor of mass-diameter relationship calculated as a function of the
17		temperature and $\beta_\sigma$ (equations 17 and 18)
18	$\beta$	Exponent of mass-diameter relationship in general
19	$\beta_T$	Exponent of mass-diameter relationship calculated calculated in function of the
20		temperature (equations 21 and 22)
21	$\beta_\sigma$	Exponent of mass-diameter relationship calculated from equation 6
22	$A_r$	Area ratio: projected surface divided by $(\pi/4 * D_{\text{max}}^2)$
23	$A_s$	Mean aspect ratio for a given $D_{\text{max}}$ (=width/ $D_{\text{max}}$ )
24	$A_sD$	Aspect ratio distribution
25	$\overline{A_s}$	Mean aspect ratio of all valid 2D images recorded during a 5s time period
26	BRAIN	Bayesian rain rate retrieval algorithm including neural network
27	CPI	Cloud particle imager, SPEC, Inc.

1	CWC	Condensed water content (in general)
2	$CWC_{B\&L}$	CWC deduced from the Baker and Lawson scheme
3	$CWC(\alpha_\sigma, \beta_\sigma)$	CWC calculated with $\alpha_\sigma$ and $\beta_\sigma$
4	$CWC(\alpha_T, \beta_T)$	CWC calculated with $\alpha_T$ and $\beta_T$
5	$CWC(\alpha_{\beta,T}, \beta_\sigma)$	CWC calculated with $\alpha_{\beta,T}$ and $\beta_\sigma$
6	$D_{max}$	Maximum length of the 2D images of the hydrometeors
7	$\Delta D_{max}$	Bin resolution of the size distribution
8	$D_{T-matrix}$	Diameter of an oblate spheroid used by the T-matrix method
9	$\Delta CWC_{max}$	Uncertainty of the retrieved CWC from RASTA reflectivity and 2D imagery of
10		OAP
11	$error_Z$	Absolute error using Z-CWC power fit and the retrieved CWC
12	$error_{Z,T}$	Absolute error using Z-CWC-T power fit and the retrieved CWC
13	$f_{ice}$	Ice fraction used for the calculation of the backscattering properties of the
14		hydrometeors
15	MADRAS	Microwave analysis & detection of rain & atmospheric systems
16	$m(D)$	Mass-diameter relationship
17	MT2010	Megha-Tropiques Falcon 20 measurement campaign (Niger, August 2010)
18	MT2011	Megha-Tropiques Falcon 20 measurement campaign (Gan, November-
19		December 2011)
20	$N_{2D-S}$	Number concentration of hydrometeors counted by the 2D-S
21	$N_{PIP}$	Number concentration of hydrometeors counted by the PIP
22	$N$	Number concentration of hydrometeors
23	$N_t$	Total number concentration of hydrometeors
24	OAP	Optical array probe
25	$P_i$	Probability distribution function used to calculate the average aspect ratio
26	PIP	Precipitation Imaging Probe

1	PSD	Particle Size Distribution
2	RASTA	French acronym for Radar Aéroporté et Sol de Télédétection des propriétés
3		nuAgeuse
4	$\rho_{ice}$	Ice density: $0.917 \text{ g cm}^{-3}$
5	S(D)	Surface-diameter relationship or area-diameter relationship
6	$\sigma$	Exponent of surface-diameter relationship in general
7	$\sigma_{2D-S}$	Exponent of surface-diameter relationship from the 2D-S 2Dimages
8	$\sigma_{PIP}$	Exponent of surface-diameter relationship from the PIP 2D images
9	Sp	Projected surface of a hydrometeor recorded by an OAP
10	T	Temperature in Kelvin
11	$Q_{back}$	Total backscattering coefficient as a function of $D_{max}$ per bin
12	Z	RASTA reflectivity at 94GHz
13	Z-CWC	fitted power law between reflectivity and CWC
14	Z-CWC-T	fitted power law between reflectivity and CWC, adding a temperature
15		dependency parametrisation

16

## 17 **Acknowledgments**

18 The authors are particularly grateful to CNES for funding the aircraft measurement campaigns  
 19 within the Megha-Tropiques project. Furthermore, we would like to thank SAFIRE for  
 20 operating the French Falcon 20 research aircraft during the two campaigns.

21

## 22 **References**

- 23 Bailey, M., and J. Hallett, 2004: Growth Rates and Habits of Ice Crystals between  $-20^\circ$  and  
 24  $-70^\circ\text{C}$ . *J. Atmospheric Sci.*, **61**, 514–544, doi:10.1175/1520-  
 25 0469(2004)061<0514:GRAHOI>2.0.CO;2.
- 26 Bailey, M. P., and J. Hallett, 2009: A Comprehensive Habit Diagram for Atmospheric Ice  
 27 Crystals: Confirmation from the Laboratory, AIRS II, and Other Field Studies. *J.*  
 28 *Atmospheric Sci.*, **66**, 2888–2899, doi:10.1175/2009JAS2883.1.

- 1 Baker, B., and R. P. Lawson, 2006: Improvement in Determination of Ice Water Content from  
2 Two-Dimensional Particle Imagery. Part I: Image-to-Mass Relationships. *J. Appl.*  
3 *Meteorol. Climatol.*, **45**, 1282–1290, doi:10.1175/JAM2398.1.
- 4 Baumgardner, D., and A. Korolev, 1997: Airspeed Corrections for Optical Array Probe  
5 Sample Volumes. *J. Atmospheric Ocean. Technol.*, **14**, 1224–1229, doi:10.1175/1520-  
6 0426(1997)014<1224:ACFOAP>2.0.CO;2.
- 7 Brown, P. R. A., and P. N. Francis, 1995: Improved Measurements of the Ice Water Content  
8 in Cirrus Using a Total-Water Probe. *J. Atmospheric Ocean. Technol.*, **12**, 410–414,  
9 doi:10.1175/1520-0426(1995)012<0410:IMOTIW>2.0.CO;2.
- 10 Cetrone, J., and R. A. Houze, 2009: Anvil clouds of tropical mesoscale convective systems in  
11 monsoon regions. *Q. J. R. Meteorol. Soc.*, **135**, 305–317, doi:10.1002/qj.389.
- 12 Field, P. R., A. J. Heymsfield, and A. Bansemer, 2006: Shattering and Particle Interarrival  
13 Times Measured by Optical Array Probes in Ice Clouds. *J. Atmospheric Ocean.*  
14 *Technol.*, **23**, 1357–1371, doi:10.1175/JTECH1922.1.
- 15 Frey, W., and Coauthors, 2011: In situ measurements of tropical cloud properties in the West  
16 African Monsoon: upper tropospheric ice clouds, Mesoscale Convective System  
17 outflow, and subvisual cirrus. *Atmospheric Chem. Phys.*, **11**, 5569–5590,  
18 doi:10.5194/acp-11-5569-2011.
- 19 Heymsfield, A. J., and J. L. Parrish, 1978: A Computational Technique for Increasing the  
20 Effective Sampling Volume of the PMS Two-Dimensional Particle Size Spectrometer.  
21 *J. Appl. Meteorol.*, **17**, 1566–1572, doi:10.1175/1520-  
22 0450(1978)017<1566:ACTFIT>2.0.CO;2.
- 23 Heymsfield, A. J., and C. D. Westbrook, 2010: Advances in the Estimation of Ice Particle Fall  
24 Speeds Using Laboratory and Field Measurements. *J. Atmospheric Sci.*, **67**, 2469–  
25 2482, doi:10.1175/2010JAS3379.1.
- 26 Heymsfield, A. J., S. Lewis, A. Bansemer, J. Iaquinta, L. M. Miloshevich, M. Kajikawa, C.  
27 Twohy, and M. R. Poellot, 2002: A General Approach for Deriving the Properties of  
28 Cirrus and Stratiform Ice Cloud Particles. *J. Atmospheric Sci.*, **59**, 3–29,  
29 doi:10.1175/1520-0469(2002)059<0003:AGAFDT>2.0.CO;2.
- 30 Heymsfield, A. J., Z. Wang, and S. Matrosov, 2005: Improved Radar Ice Water Content  
31 Retrieval Algorithms Using Coincident Microphysical and Radar Measurements. *J.*  
32 *Appl. Meteorol.*, **44**, 1391–1412, doi:10.1175/JAM2282.1.
- 33 Heymsfield, A. J., C. Schmitt, A. Bansemer, and C. H. Twohy, 2010a: Improved  
34 Representation of Ice Particle Masses Based on Observations in Natural Clouds. *J.*  
35 *Atmospheric Sci.*, **67**, 3303–3318, doi:10.1175/2010JAS3507.1.
- 36 Heymsfield, G. M., L. Tian, A. J. Heymsfield, L. Li, and S. Guimond, 2010b: Characteristics  
37 of Deep Tropical and Subtropical Convection from Nadir-Viewing High-Altitude  
38 Airborne Doppler Radar. *J. Atmospheric Sci.*, **67**, 285–308,  
39 doi:10.1175/2009JAS3132.1.

- 1 Hogan, R. J., M. P. Mittermaier, and A. J. Illingworth, 2006: The Retrieval of Ice Water  
2 Content from Radar Reflectivity Factor and Temperature and Its Use in Evaluating a  
3 Mesoscale Model. *J. Appl. Meteorol. Climatol.*, **45**, 301–317,  
4 doi:10.1175/JAM2340.1.
- 5 Hogan, R. J., L. Tian, P. R. A. Brown, C. D. Westbrook, A. J. Heymsfield, and J. D.  
6 Eastment, 2011: Radar Scattering from Ice Aggregates Using the Horizontally  
7 Aligned Oblate Spheroid Approximation. *J. Appl. Meteorol. Climatol.*, **51**, 655–671,  
8 doi:10.1175/JAMC-D-11-074.1.
- 9 Houze, R. A., 2004: Mesoscale convective systems. *Rev. Geophys.*, **42**, n/a–n/a,  
10 doi:10.1029/2004RG000150.
- 11 Huffman, G. J., R. F. Adler, D. T. Bolvin, G. Gu, E. J. Nelkin, K. P. Bowman Y. Hong, E. F.  
12 Stocker, and D. B. Wolff, 2007: The TRMM Multisatellite Precipitation Analysis  
13 (TMPA): Quasi-Global, Multiyear, Combined-Sensor Precipitation Estimates at Fine  
14 Scales. *J. Hydrometeorol.*, **8**, 38–55, doi:10.1175/JHM560.1.
- 15 Jensen, E., D. Starr, and O. B. Toon, 2004: Mission investigates tropical cirrus clouds. *Eos*  
16 *Trans. Am. Geophys. Union*, **85**, 45–50, doi:10.1029/2004EO050002.
- 17 Jensen, M. P., and A. D. Del Genio, 2003: Radiative and Microphysical Characteristics of  
18 Deep Convective Systems in the Tropical Western Pacific. *J. Appl. Meteorol.*, **42**,  
19 1234–1254, doi:10.1175/1520-0450(2003)042<1234:RAMCOD>2.0.CO;2.
- 20 Kobayashi, R., 1993: Modeling and numerical simulations of dendritic crystal growth. *Phys.*  
21 *Nonlinear Phenom.*, **63**, 410–423, doi:10.1016/0167-2789(93)90120-P.
- 22 Liu, C.-L., and A. J. Illingworth, 2000: Toward More Accurate Retrievals of Ice Water  
23 Content from Radar Measurements of Clouds. *J. Appl. Meteorol.*, **39**, 1130–1146,  
24 doi:10.1175/1520-0450(2000)039<1130:TMAROI>2.0.CO;2.
- 25 Locatelli, J. D., and P. V. Hobbs, 1974: Fall speeds and masses of solid precipitation particles.  
26 *J. Geophys. Res.*, **79**, 2185–2197, doi:10.1029/JC079i015p02185.
- 27 Maxwell Garnet, J. C., 1904: Colours in Metal Glasses and in Metallic Films. *Philos. Trans.*  
28 *R. Soc.*, 385–420, doi:10.1098/rsta.1904.0024.
- 29 McFarquhar, G. M., M. S. Timlin, R. M. Rauber, B. F. Jewett, J. A. Grim, and D. P.  
30 Jorgensen, 2007: Vertical Variability of Cloud Hydrometeors in the Stratiform Region  
31 of Mesoscale Convective Systems and Bow Echoes. *Mon. Weather Rev.*, **135**, 3405–  
32 3428, doi:10.1175/MWR3444.1.
- 33 Mishchenko, M. I., L. D. Travis, and D. W. Mackowski, 1996: T-matrix computations of light  
34 scattering by nonspherical particles: A review. *J. Quant. Spectrosc. Radiat. Transf.*,  
35 **55**, 535 – 575, doi:10.1016/0022-4073(96)00002-7.
- 36 Mitchell, D. L., 1996: Use of Mass- and Area-Dimensional Power Laws for Determining  
37 Precipitation Particle Terminal Velocities. *J Atmos Sci*, **53**, 1710–1723,  
38 doi:10.1175/1520-0469(1996)053<1710:UOMAAD>2.0.CO;2.

- 1 Mitchell, D. L., R. Zhang, and R. L. Pitter, 1990: Mass-Dimensional Relationships for Ice  
2 Particles and the Influence of Riming on Snowfall Rates. *J. Appl. Meteorol.*, **29**, 153–  
3 163, doi:10.1175/1520-0450(1990)029<0153:MDRFIP>2.0.CO;2.
- 4 Nicholls, S., J. Leighton, and R. Barker, 1990: A New Fast Response Instrument for  
5 Measuring Total Water Content from Aircraft. *J. Atmospheric Ocean. Technol.*, **7**,  
6 706–718, doi:10.1175/1520-0426(1990)007<0706:ANFRIF>2.0.CO;2.
- 7 Ogren, J. A., J. Heintzenberg, and R. J. Charlson, 1985: In-situ sampling of clouds with a  
8 droplet to aerosol converter. *Geophys. Res. Lett.*, **12**, 121–124,  
9 doi:10.1029/GL012i003p00121.
- 10 Protat, A., and C. R. Williams, 2011: The Accuracy of Radar Estimates of Ice Terminal Fall  
11 Speed from Vertically Pointing Doppler Radar Measurements. *J. Appl. Meteorol.*  
12 *Climatol.*, **50**, 2120–2138, doi:10.1175/JAMC-D-10-05031.1.
- 13 Protat, A., J. Delanoë, D. Bouniol, A. J. Heymsfield, A. Bansemmer, and P. Brown, 2007:  
14 Evaluation of Ice Water Content Retrievals from Cloud Radar Reflectivity and  
15 Temperature Using a Large Airborne In Situ Microphysical Database. *J. Appl.*  
16 *Meteorol. Climatol.*, **46**, 557–572, doi:10.1175/JAM2488.1.
- 17 Protat, A., J. Delnoë, P. T. May, A. Plana-Fattori, A. Hasson, E. O'Connor, U. Görndorf, and  
18 A. J. Heymsfield, 2009: Assessment of Cloudsat Reflectivity Measurements and Ice  
19 Cloud Properties Using Ground-Based and Airborne Cloud Radar Observations. *J.*  
20 *Atmospheric Ocean. Technol.*, **26**, 1717–1741, doi:10.1175/2009JTECHA1246.1.
- 21 Schmitt, C. G., and A. J. Heymsfield, 2010: The Dimensional Characteristics of Ice Crystal  
22 Aggregates from Fractal Geometry. *J. Atmospheric Sci.*, **67**, 1605–1616,  
23 doi:10.1175/2009JAS3187.1.
- 24 Spencer, R. W., H. M. Goodman, and R. E. Hood, 1989: Precipitation Retrieval over Land  
25 and Ocean with the SSM/I: Identification and Characteristics of the Scattering Signal.  
26 *J. Atmospheric Ocean. Technol.*, **6**, 254–273, doi:10.1175/1520-  
27 0426(1989)006<0254:PROLAO>2.0.CO;2.
- 28 Tang, D., and A. G. Marangoni, 2006: 3D fractal dimension of fat crystal networks. *Chem.*  
29 *Phys. Lett.*, **433**, 248 – 252, doi:http://dx.doi.org/10.1016/j.cplett.2006.11.057.
- 30 Toon, O. B., D.O. Star, E.J. Jensen, P.A. Newman, S. Platnick, M.R. Schoeberl, P.O.  
31 Wennberg, S.C. Wofsy, M.J. Kurylo, H. Maring, K.W. Jucks, M.S. Craig, M.F.  
32 Vasques, L. Pfister, K.H. Rosenlof, H.B. Selkirk, P.R. Colarco, S.R. Kawa, G.G.  
33 Mace, P. Minnis and K.E. Pickering, 2010: Planning, implementation, and first results  
34 of the Tropical Composition, Cloud and Climate Coupling Experiment (TC4). *J.*  
35 *Geophys. Res. Atmospheres*, **115**, n/a–n/a, doi:10.1029/2009JD013073.
- 36 Viltard, N., C. Burlaud, and C. D. Kummerow, 2006: Rain Retrieval from TMI Brightness  
37 Temperature Measurements Using a TRMM PR–Based Database. *J. Appl. Meteorol.*  
38 *Climatol.*, **45**, 455–466, doi:10.1175/JAM2346.1.

1 Westbrook, C. D., R. C. Ball, P. R. Field, and A. J. Heymsfield, 2004: Theory of growth by  
2 differential sedimentation, with application to snowflake formation. *Phys Rev E*, **70**,  
3 021403, doi:10.1103/PhysRevE.70.021403.

4 Zikmunda, J., and G. Vali, 1972: Fall Patterns and Fall Velocities of Rimed Ice Crystals. *J.*  
5 *Atmospheric Sci.*, **29**, 1334–1347, doi:10.1175/1520-  
6 0469(1972)029<1334:FPAFVO>2.0.CO;2.

7 Zipser, E. J., C.H. Twohy, S-C. Tsay, N.C. Hsu, G.M. Heymsfield, K.L. Thornhill, S. Taneli,  
8 R. Robert, T.N. Krishnamurti, Q. Ji, G. Jenkins, S. Ismail, R. Ferrare, G. Chen, E.V.  
9 Browell, B. Anderson, R. Hood, H.M. Goodman, A.J. Heymsfield, J. Halverson, J.P.  
10 Dunion, M. Douglas and R. Cifelli, 2009: The Saharan Air Layer and the Fate of  
11 African Easterly Waves—NASA’s AMMA Field Study of Tropical Cyclogenesis.  
12 *Bull. Am. Meteorol. Soc.*, **90**, 1137–1156, doi:10.1175/2009BAMS2728.1.

13

14









































1 TABLE 1. List of Falcon 20 research flights used in this study.




























Flight program	Flight number	Day	Hour (UTC)	Cloud type
MT2010 Continental	Flight 15	2010/08/06	1610-1900	MCS squall line
	Flight 17	2010/08/10	0845-1160	MCS squall line
	Flight 18	2010/08/13	1320-1625	MCS squall line
	Flight 19	2010/08/17	1030-1340	MCS squall line
	Flight 20	2010/08/17	2335-0240	MCS squall line
MT2011 Oceanic	Flight 45	2011/11/27	0530-0850	MCS ITCZ
	Flight 46	2011/11/27	1515-1825	MCS ITCZ
	Flight 49	2011/12/06	1325-1540	Isolated Convective System
	Flight 50	2011/12/08	0600-0900	Isolated Convective System

2

3

1 TABLE 2. Ice crystal types and corresponding exponents  $\sigma$  and  $\beta$  of  $S(D)$  and  $m(D)$  relations.  
2 The symbols in the left column are subsequently used in Fig. 4 for individual ice crystal  
3 shapes. The first part of the table stems from Mitchell (1996) where random orientation is  
4 assumed for particles with  $D_{\max} < 100\mu\text{m}$  and horizontal orientation is assumed for particles  
5 beyond  $100\mu\text{m}$ . The second part of the table stems from simulations.

symbol	Description	Range	$\sigma$	$\beta$
<b>Ice crystal shapes from Mitchell (1996)</b>				
	hexagonal plates	$15\mu\text{m} < D_{\max} < 100\mu\text{m}$	1.85	2.45
	hexagonal plates	$100 < D_{\max} < 300\mu\text{m}$	2	2.45
	hexagonal columns	$30 < D_{\max} < 100\mu\text{m}$	2	2.91
	hexagonal columns	$100 < D_{\max} < 300\mu\text{m}$	1.5	1.91
	hexagonal columns	$D_{\max} > 300\mu\text{m}$	1.41	1.74
	rimed long columns	$200 < D_{\max} < 2400\mu\text{m}$	1.41	1.8
	crystals with sector-like branches (P1b)	$10 < D_{\max} < 40\mu\text{m}$	1.85	2.42
	crystals with sector-like branches (P1b)	$40 < D_{\max} < 2000\mu\text{m}$	1.97	2.02
	broad-branched crystals (Plc)	$10 < D_{\max} < 100\mu\text{m}$	1.85	2.42
	broad-branched crystals (Plc)	$100 < D_{\max} < 1000\mu\text{m}$	1.76	1.8
	stellar crystals with broad arms (P1d)	$10 < D_{\max} < 90\mu\text{m}$	1.85	2.42
	stellar crystals with broad arms (P1d)	$90 < D_{\max} < 1500\mu\text{m}$	1.63	1.67
	densely rimed dendrites (R2b)	$1800 < D_{\max} < 4000\mu\text{m}$	1.76	2.3
	side planes (S1)	$300 < D_{\max} < 2500\mu\text{m}$	1.88	2.3
	bullet rosettes, 5 branches at $-42^\circ\text{C}$	$200 < D_{\max} < 1000\mu\text{m}$	1.57	2.26
	aggregates of side planes	$600 < D_{\max} < 4100\mu\text{m}$	1.88	2.2
	aggregates of side planes, columns & bullets (S3)	$800 < D_{\max} < 4500\mu\text{m}$	1.88	2.1
	assemblies of planar poly-crystals in cirrus clouds	$20 < D_{\max} < 450\mu\text{m}$	1.88	2.45
	lump graupel (R4b)	$500 < D_{\max} < 3000\mu\text{m}$	2	2.8
	hail	$5000 < D_{\max} < 25000\mu\text{m}$	2	3
<b>Simulations of Ice-Crystals shape</b>				
	columns ( $H=5*L$ )	$100 < D_{\max} < 1000\mu\text{m}$	1.86	2.53
	columns ( $H=10*L$ )	$100 < D_{\max} < 1000\mu\text{m}$	1.87	2.44
	columns ( $L=160\mu\text{m}$ )	$100 < D_{\max} < 1000\mu\text{m}$	1.06	1.04
	columns ( $L = \sqrt{H}$ )	$100 < D_{\max} < 1000\mu\text{m}$	1.48	1.78
	thick star ( $H = 0.2*L$ )	$200 < D_{\max} < 1200\mu\text{m}$	1.98	2.89
	thick star ( $H = 0.1*L$ )	$200 < D_{\max} < 1200\mu\text{m}$	1.99	2.86
	thick stars ( $H=40\mu\text{m}$ )	$200 < D_{\max} < 1200\mu\text{m}$	1.49	2.06
	thick stars ( $H = \sqrt{L}$ )	$200 < D_{\max} < 1200\mu\text{m}$	1.76	2.48
	thin Stars ( $H=0.2*L$ )	$100 < D_{\max} < 1000\mu\text{m}$	1.96	2.89
	thin Stars ( $H=0.1*L$ )	$100 < D_{\max} < 1000\mu\text{m}$	1.94	2.75
	Thin Stars ( $H=40\mu\text{m}$ )	$100 < D_{\max} < 1000\mu\text{m}$	1.39	2.06
	thin Stars ( $H = \sqrt{L}$ )	$100 < D_{\max} < 1000\mu\text{m}$	1.74	2.51
	plates ( $H= 0.2*L$ )	$200 < D_{\max} < 2000\mu\text{m}$	1.95	2.96
	plates ( $H = 0.1*L$ )	$200 < D_{\max} < 2000\mu\text{m}$	1.92	2.91
	plates ( $H=40\mu\text{m}$ )	$200 < D_{\max} < 2000\mu\text{m}$	1.65	2.03
	plates ( $H = \sqrt{L}$ )	$200 < D_{\max} < 2000\mu\text{m}$	1.86	2.49
	Rosettes ( $L= 50\mu\text{m}$ ; $N_{\max}=3$ )	$50 < D_{\max} < 500\mu\text{m}$	1.37	1.04
	Rosettes ( $L = \sqrt{H}$ ; $N_{\max}=3$ )	$50 < D_{\max} < 500\mu\text{m}$	1.69	2.21

	Rosettes ( $L=100\mu\text{m}$ ; $N_{\text{max}}=4$ )	$100 < D_{\text{max}} < 1000\mu\text{m}$	1.39	1.26
	Rosettes ( $L = \sqrt{H}$ ; $N_{\text{max}}=4$ )	$100 < D_{\text{max}} < 1000\mu\text{m}$	1.65	2.16
	Rosettes ( $L=0.5H$ ; $N_{\text{max}}=5$ )	$500 < D_{\text{max}} < 2000\mu\text{m}$	1.83	2.9
	Rosettes ( $L=0.25H$ ; $N_{\text{max}}=6$ )	$500 < D_{\text{max}} < 2500\mu\text{m}$	1.78	2.97
	Rosettes( $L=100\mu\text{m}$ ; $N_{\text{max}}=6$ )	$100 < D_{\text{max}} < 1000\mu\text{m}$	1.42	1.25
	Rosettes( $L = \sqrt{H}$ ; $N_{\text{max}}=6$ )	$100 < D_{\text{max}} < 1000\mu\text{m}$	1.66	2.16
	Capped columns (2 thick stars: $L_2=2.5L_1$ ; $H= L_1$ )	$150 < D_{\text{max}} < 1400\mu\text{m}$	1.79	2.21
	Capped columns (2 plates: $L_2=2.5L_1$ ; $H= L_1$ )	$150 < D_{\text{max}} < 1400\mu\text{m}$	1.92	2.43
	$8 < N_{\text{agg}} < 30$ thick stars ( $H = \sqrt{L}$ ) Individual Diameter such : $300 < L < 400\mu\text{m}$	$1000 < D_{\text{max}} < 4000$	1.79	1.92
	$8 < N_{\text{agg}} < 30$ plates ( $H = 0.1 * L$ ) Individual Diameter such : $200 < L < 300\mu\text{m}$	$600 < D_{\text{max}} < 2000$	1.8	1.81
	$8 < N_{\text{agg}} < 30$ plates ( $H = \sqrt{L}$ ) Individual Diameter such : $200 < L < 300\mu\text{m}$	$600 < D_{\text{max}} < 2500$	1.59	1.69
	$2 < N_{\text{agg}} < 4$ ; columns ( $L=160\mu\text{m}$ ) Individual Diameter such : $400 < H < 600$	$400 < D_{\text{max}} < 1500$	1.26	1.75
	$2 < N_{\text{agg}} < 4$ ; columns ( $L = \sqrt{H}$ ) Individual Diameter such : $400 < H < 600$	$200 < D_{\text{max}} < 1000$	1.45	2.07
	$2 < N_{\text{agg}} < 4$ ; thick stars ( $H= 0.2 * L$ ) Individual Diameter such : $400 < L < 600\mu\text{m}$	$400 < D_{\text{max}} < 3000$	1.82	2.62
	$2 < N_{\text{agg}} < 4$ ; thick stars ( $H= 0.1 * L$ ) Individual Diameter such : $400 < L < 600\mu\text{m}$	$400 < D_{\text{max}} < 3000$	1.63	2.62
	$2 < N_{\text{agg}} < 4$ ; thick stars ( $H= 40\mu\text{m}$ ) Individual Diameter such : $400 < L < 600\mu\text{m}$	$400 < D_{\text{max}} < 3000$	1.87	2.25
	$2 < N_{\text{agg}} < 4$ ; thick stars ( $H = \sqrt{L}$ ) Individual Diameter such : $400 < L < 600\mu\text{m}$	$400 < D_{\text{max}} < 3000$	1.72	2.46
	$2 < N_{\text{agg}} < 4$ ; thin stars ( $H= 0.2 * L$ ) Individual Diameter such : $300 < L < 600\mu\text{m}$	$300 < D_{\text{max}} < 2000$	1.64	2.52
	$2 < N_{\text{agg}} < 4$ ; thin stars ( $H= 0.1 * L$ ) Individual Diameter such : $300 < L < 500\mu\text{m}$	$300 < D_{\text{max}} < 1500$	1.72	2.52
	$2 < N_{\text{agg}} < 4$ ; thin stars ( $H= 40\mu\text{m}$ ) Individual Diameter such : $300 < L < 500\mu\text{m}$	$300 < D_{\text{max}} < 1500$	1.46	2.14
	$2 < N_{\text{agg}} < 4$ ; thin stars ( $H = \sqrt{L}$ ) Individual Diameter such : $300 < L < 500\mu\text{m}$	$300 < D_{\text{max}} < 2000$	1.53	2.37
	$2 < N_{\text{agg}} < 4$ ; plates ( $H= 0.2 * L$ ) Individual Diameter such : $300 < L < 500\mu\text{m}$	$300 < D_{\text{max}} < 2000$	1.87	2.57
	$2 < N_{\text{agg}} < 4$ ; plates ( $H= 0.1 * L$ ) Individual Diameter such : $300 < L < 500\mu\text{m}$	$300 < D_{\text{max}} < 1500$	1.61	2.37
	$2 < N_{\text{agg}} < 4$ ; plates ( $H= 40\mu\text{m}$ ) Individual Diameter such : $300 < L < 500\mu\text{m}$	$300 < D_{\text{max}} < 1500$	1.64	1.99
	$2 < N_{\text{agg}} < 4$ ; plates ( $H = \sqrt{L}$ ) Individual Diameter such : $300 < L < 600\mu\text{m}$	$300 < D_{\text{max}} < 1500$	1.76	2.29
	$3 < N_{\text{agg}} < 20$ ; spheres Individual Diameter such : $D = 60\mu\text{m}$ ;	$200 < D_{\text{max}} < 2000\mu\text{m}$	1.45	1.74
	$3 < N_{\text{agg}} < 50$ ; spheres Individual Diameter such : $D = 150\mu\text{m}$ ;	$100 < D_{\text{max}} < 1000\mu\text{m}$	1.54	1.84

1 TABLE 3. Uncertainty of retrieved  $\alpha$  and CWC as a function of the uncertainty of the measured  
 2 reflectivity.

$\Delta Z$ [dBZ]	$\Delta\alpha$ (%)	$\Delta CWC$ (%)
-2	-26	-26
-1	-12	-12
+1	+11	+11
+2	+21	+21

3

4 TABLE 4. Uncertainty of retrieved  $\alpha$  and CWC as a function of the uncertainty of the average  
 5 aspect ratio of 2D images.

$\overline{\Delta A_s}$ (%)	$\Delta\alpha$ (%)	$\Delta CWC$ (%)
-20	-12	-12
-10	-6	-6
+10	+6	+6
+20	+13	+13

6

7 TABLE 5. Ratios of fitted  $\alpha_\beta$  and  $\alpha_{\beta,T}$  over retrieved  $\alpha_\sigma$  from T-matrix calculations. Average  
 8 ratios are given in column E. Quartile, median, third quartile, are given in 1/4, 1/2, and 3/4  
 9 columns.

	E	1/4	1/2	3/4
MT2010 : $\alpha_\beta/\alpha_\sigma$	1.07	0.66	1.03	1.47
MT2011 : $\alpha_\beta/\alpha_\sigma$	1.03	0.54	0.95	1.53
MT2010 : $\alpha_{\beta,T}/\alpha_\sigma$	1.08	0.91	1.03	1.20
MT2011 : $\alpha_{\beta,T}/\alpha_\sigma$	0.99	0.74	0.92	1.13

10

1 TABLE 6. Ratio of fitted  $\alpha_T$  over retrieved  $\alpha_\sigma$ , and of  $CWC(\alpha_T, \beta_T)$  calculated from fitted  $\alpha_T$   
2 and  $\beta_T$  over  $CWC(\alpha_\sigma, \beta_\sigma)$  calculated with T-matrix retrieved  $\alpha_\sigma$  and  $\beta_\sigma$ . In addition, differences  
3 between  $\beta_T$  and  $\beta_\sigma$  are shown. Expected values of ratios and differences are given in column  
4 E. first quartile, median, and third quartile are given in 1/4, 1/2, and 3/4 columns.

	E	1/4	1/2	3/4
MT2010 : $\alpha_T/\alpha_\sigma$	1.12	0.77	0.98	1.23
MT2010 : $\beta_T-\beta_\sigma$	-0.02	-0.14	-0.03	+0.08
MT2010: $CWC(\alpha_T, \beta_T)/CWC(\alpha_\sigma, \beta_\sigma)$	1.03	0.86	0.98	1.15
MT2011 : $\alpha_T/\alpha_\sigma$	1.35	0.61	1.01	1.60
MT2011 : $\beta_T-\beta_\sigma$	+0.03	-0.13	+0.03	+0.21
MT2011: $CWC(\alpha_T, \beta_T)/CWC(\alpha_\sigma, \beta_\sigma)$	0.94	0.70	0.90	1.09

5

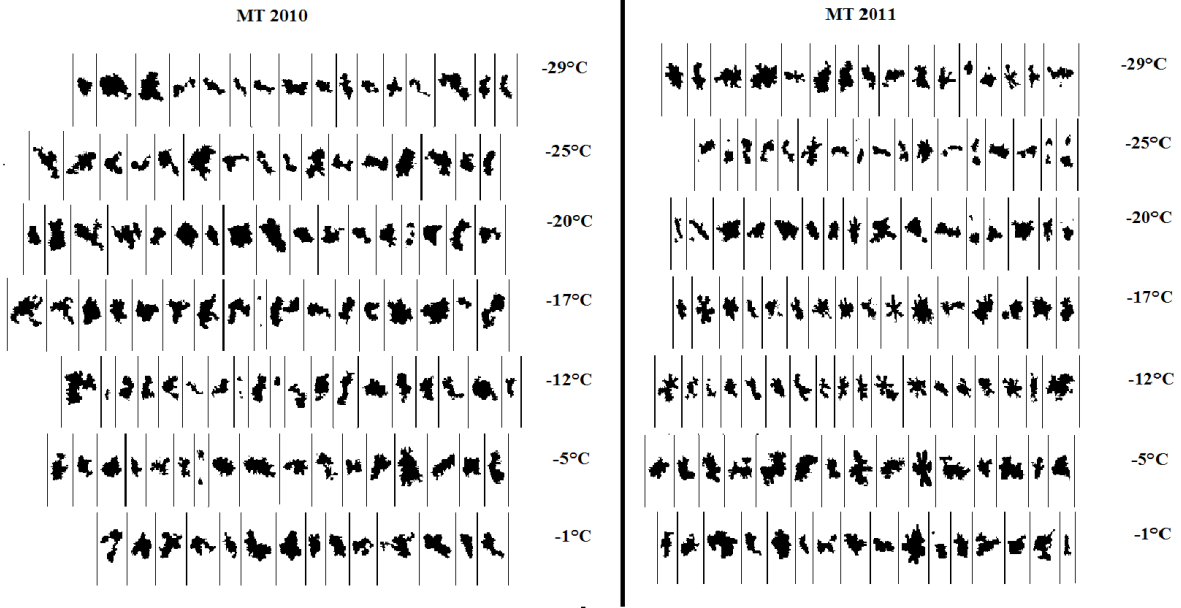
6 TABLE 7. Fitted Z-CWC and Z-CWC-T relationships according to  $CWC(\alpha, \beta)$  calculations  
7 with different methods for MT2010 and MT2011 datasets.

	CWC(Z)	CWC(Z, T)
T-matrix(MT2010)	$CWC=0.0981*Z^{0.805}$	$CWC = 0.7183*e^{-0.0078913*T} .Z^{(-0.002549*T+ 1.4813)}$
T-matrix (MT2011)	$CWC= 0.0869*Z^{0.775}$	$CWC = 18.4392*e^{-0.02115*T} .Z^{(0.002659*T+ 0.13467)}$
MT2010(equation17)	$CWC = 0.1421*Z^{0.655}$	$CWC = 0.44974*e^{-0.004527*T} .Z^{(-0.0044794*T+ 1.8224)}$
MT2011(equation18)	$CWC = 0.0893*Z^{0.682}$	$CWC = 0.93632*e^{-0.0093472*T} .Z^{(-0.0017635*T+ 1.1748)}$
mean(MT2010)(equation19)	$CWC = 0.1490*Z^{0.659}$	$CWC =62.9368*e^{-0.023757*T} .Z^{(-0.002388*T+ 1.3059)}$
mean(MT2011)(equation20)	$CWC = 0.1084*Z^{0.656}$	$CWC =65.3563*e^{-0.025176*T} .Z^{(-0.0019304*T+ 1.2195)}$
MT2010(equation21)	$CWC = 0.1261*Z^{0.686}$	$CWC = 0.3365*e^{-0.0037815*T} .Z^{(-0.0026268*T+ 1.3679)}$
MT2011(equation22)	$CWC = 0.0826*Z^{0.708}$	$CWC = 0.12055*e^{-0.0016174*T} .Z^{(-0.0021477*T+ 1.2853)}$
H10(NAMMA)	$CWC = 0.2397*Z^{0.664}$	$CWC = 446.6519*e^{-0.029602*T} .Z^{(-0.0012781*T+ 1.0319)}$
H10(cv-gt)	$CWC = 0.1101*Z^{0.662}$	$CWC = 52.153*e^{-0.024225*T} .Z^{(-0.0020589*T+ 1.2569)}$
BF95 (MT2010)	$CWC = 0.0797*Z^{0.668}$	$CWC = 856.8913*e^{-0.036509*T} .Z^{(-0.0001986*T+ 0.76656)}$
BF95 (MT2011)	$CWC = 0.0694*Z^{0.635}$	$CWC = 112.1674*e^{-0.02908*T} .Z^{(-0.00076668*T+ 0.90401)}$

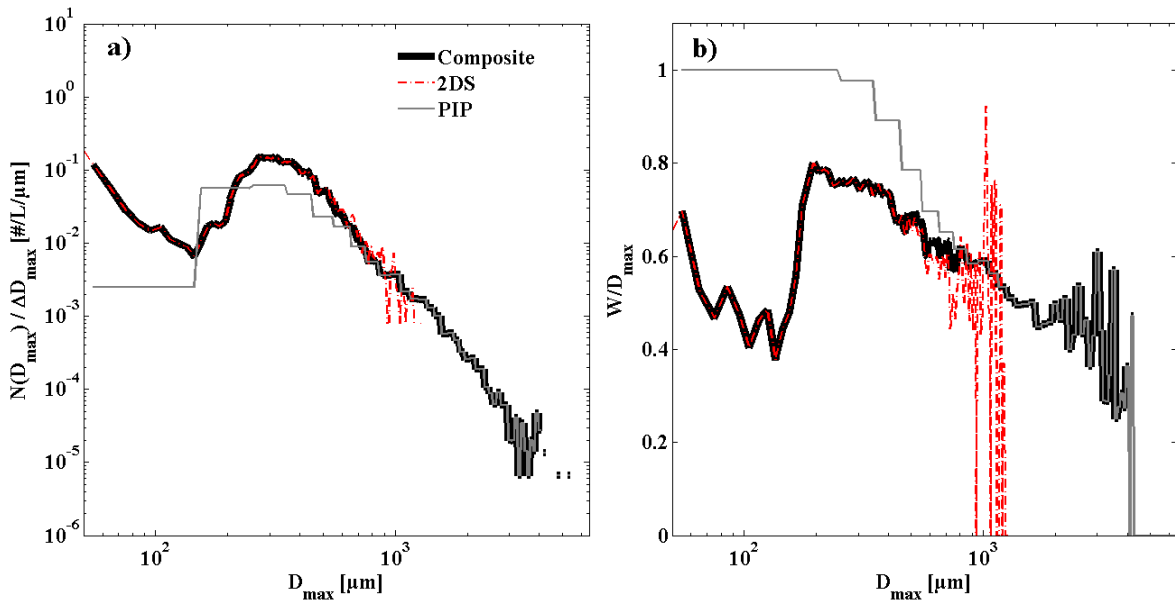
8

9 TABLE 8. For 7 different methods calculating  $CWC(\alpha, \beta)$ , for MT2010 and MT2011  
10 datasets, correlation coefficients (cc) between  $CWC(\alpha, \beta)$  and fitted  $CWC(Z)$  and  $CWC(Z, T)$ ,  
11 respectively, are shown in the left column. In addition, expected value E, 1<sup>st</sup> quartile, median,  
12 3<sup>rd</sup> quartile and 90<sup>th</sup> percentile of  $error_Z$  and  $error_{Z,T}$  are presented. Also calculated below:  
13  $error_{Z,T} - error_Z$ .

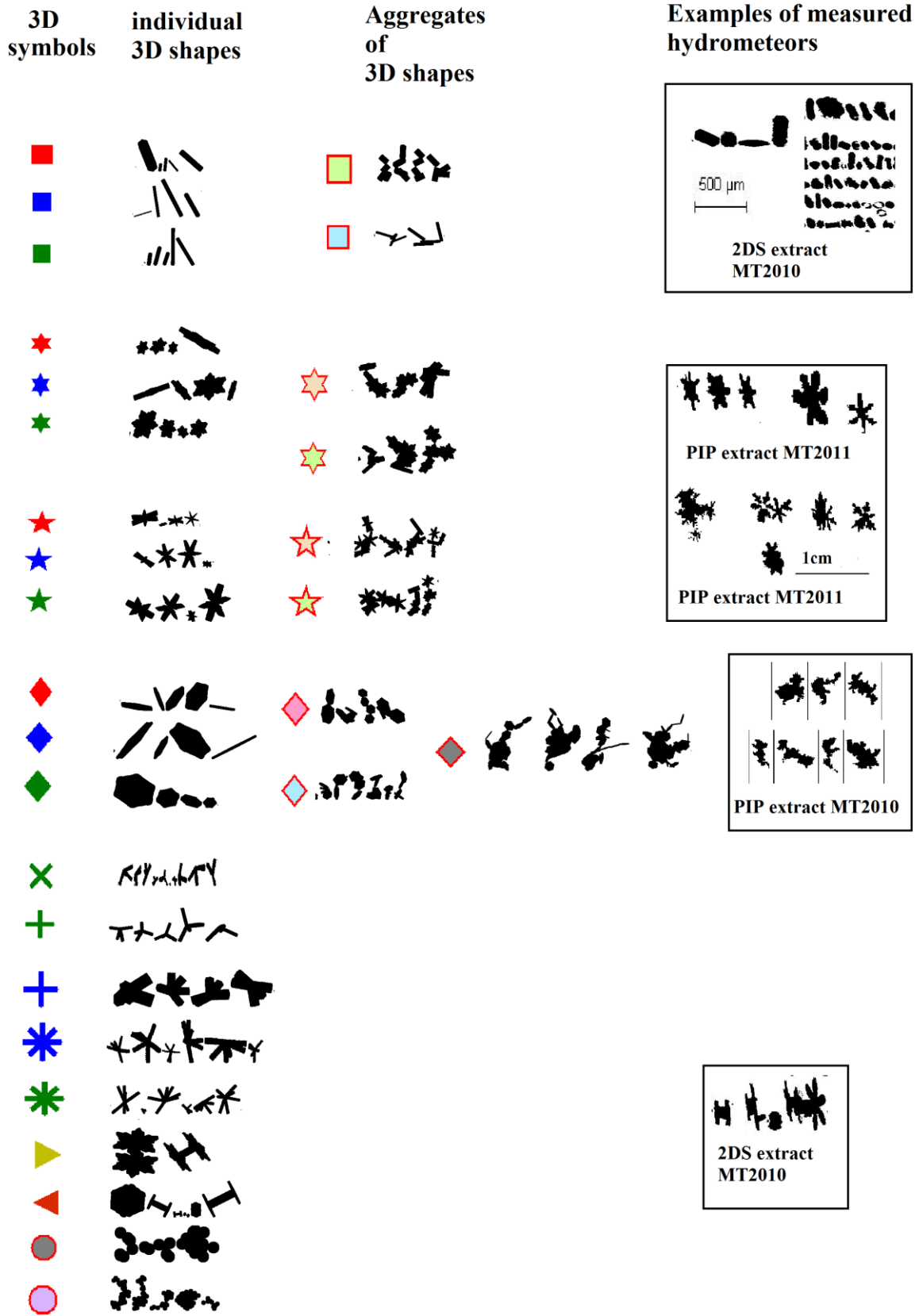
<b>CWC(Z) versus CWC(<math>\alpha</math>, <math>\beta</math>) ; error<sub>Z</sub>: E, 1/4, 1/2, 3/4, 9/10</b>						
	cc	E	1/4	1/2	3/4	9/10
T-matrix(MT2010)	0.96	24	7	15	28	52
T-matrix (MT2011)	0.95	39	14	29	48	70
MT2010(equation17)	0.86	43	12	23	41	91
MT2011(equation18)	0.86	75	18	37	62	112
mean(MT2010)(equation19)	0.85	49	15	29	48	103
mean(MT2011)(equation20)	0.85	75	20	41	63	111
MT2010(equation21)	0.89	40	11	22	40	86
MT2011(equation22)	0.87	71	17	35	60	111
H10(NAMMA)	0.84	51	15	30	49	105
H10(cv-gt)	0.85	75	20	41	62	110
BF95(MT2010)	0.83	54	16	32	53	113
BF95(MT2011)	0.84	72	20	43	65	118
<b>CWC(Z,T) versus CWC(<math>\alpha</math>, <math>\beta</math>) ; error<sub>Z,T</sub>: E, 1/4, 1/2, 3/4, 9/10</b>						
	cc	E	1/4	1/2	3/4	9/10
T-matrix(MT2010)	0.90	22	7	14	25	47
T-matrix (MT2011)	0.93	34	11	24	42	66
MT2010(equation17)	0.75	40	10	21	40	84
MT2011(equation18)	0.82	71	17	35	60	106
mean(MT2010)(equation19)	0.81	39	10	22	40	83
mean(MT2011)(equation20)	0.84	66	16	34	59	102
MT2010(equation21)	0.79	38	10	21	40	83
MT2011(equation22)	0.83	69	17	35	59	106
H10(NAMMA)	0.81	38	10	21	39	79
H10(cv-gt)	0.84	66	16	34	59	102
BF95(MT2010)	0.81	38	10	21	39	76
BF95(MT2011)	0.84	63	16	35	60	104
<b>error<sub>Z,T</sub> - error<sub>Z</sub></b>						
		E	1/4	1/2	3/4	9/10
T-matrix(MT2010)		-2	0	-1	-3	-5
T-matrix (MT2011)		-5	-3	-5	-6	-4
MT2010(equation17)		-3	-1	-1	0	-7
MT2011(equation18)		-4	-1	-2	-1	-6
mean(MT2010)(equation19)		-11	-5	-7	-8	-20
mean(MT2011)(equation20)		-9	-4	-8	-3	-10
MT2010(equation21)		-1	-1	-1	0	-3
MT2011(equation22)		-2	0	-1	0	-5
H10(NAMMA)		-13	-5	-9	-11	-26
H10(cv-gt)		-9	-4	-7	-3	-9
BF95(MT2010)		-16	-6	-11	-14	-36
BF95(MT2011)		-10	-4	-9	-5	-14



1  
2 FIG. 1. Examples of 2D images recorded by the precipitation imaging probe PIP for MT2010  
3 and MT2011. Selected hydrometeor images are presented as a function of temperature in °C  
4 and have sizes between 2mm to 4mm.

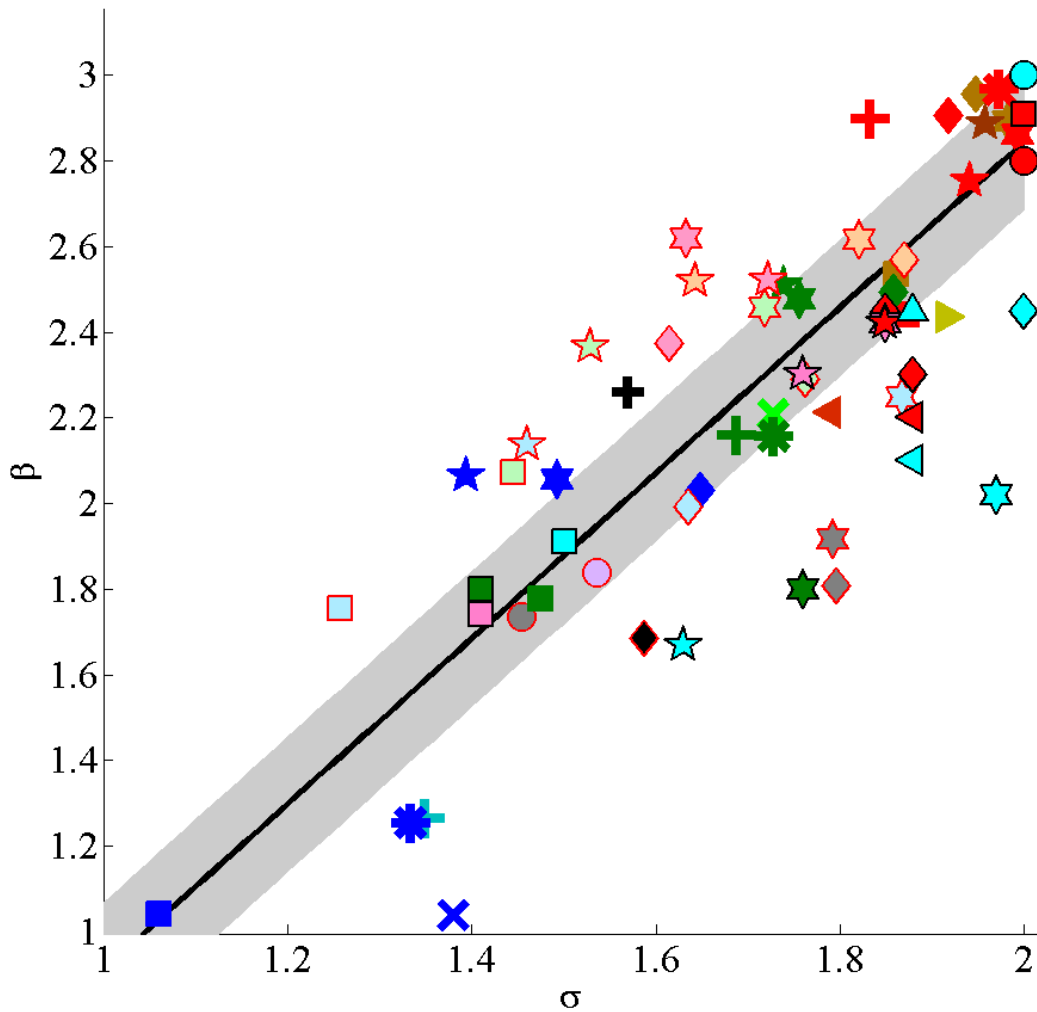


5  
6 FIG. 2. a) Number size distributions (as a function of  $D_{max}$ ) of cloud particles. The dashed red  
7 line represents the 2D-S data, the grey line the PIP data, and the bold black line represents the  
8 composite particle number size distribution (PSD). b) Aspect ratio of 2D particles as a  
9 function of  $D_{max}$ . Symbols for 2D-S and PIP as above. All curves (number size distributions  
10 and aspect ratios) represent an average over 5 seconds of measurements.



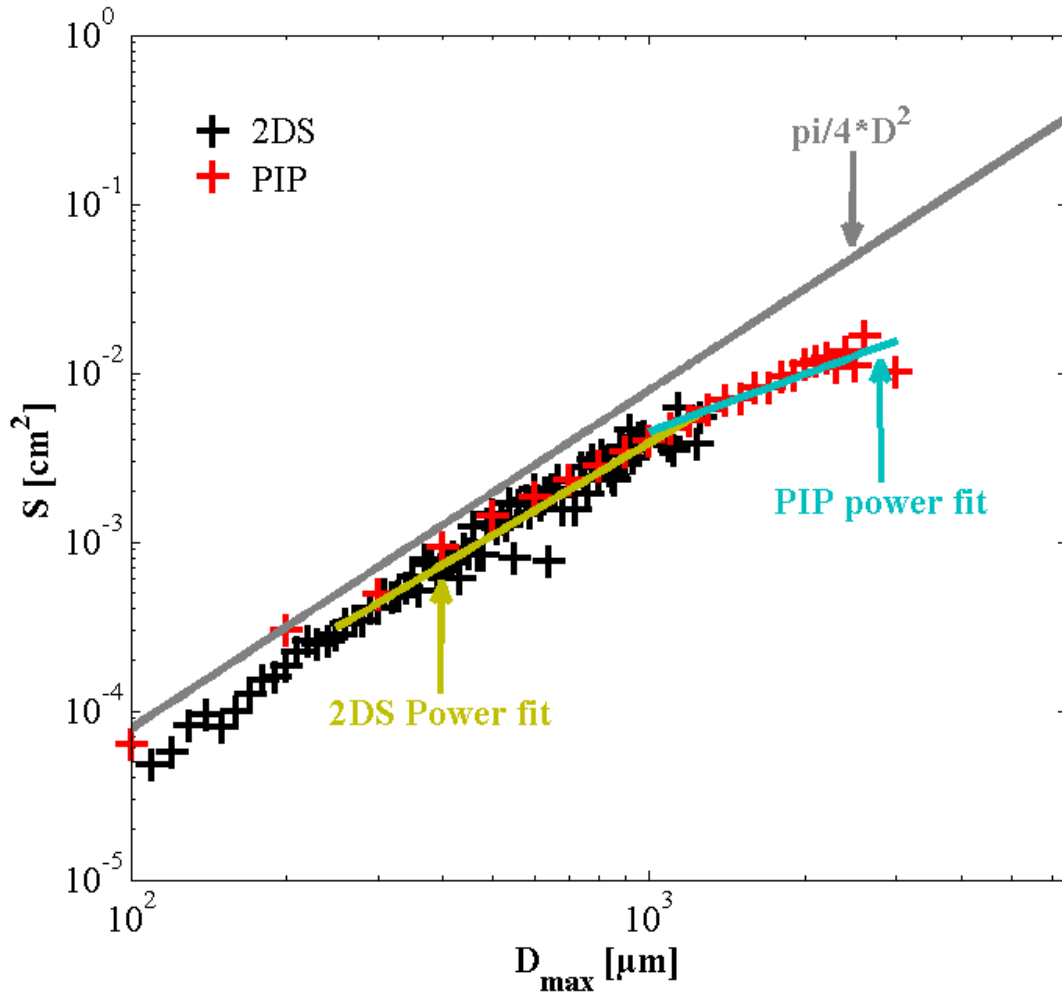


1 FIG. 3. To the left are presented examples of 2D projections of randomly oriented individual  
 2 3D shapes (single hydrometeors) with their corresponding symbols as they are used in  
 3 subsequent Fig. 4 and in Table 2. In the middle column are shown examples of aggregates  
 4 composed of respective single individual shapes to the left. The right column shows examples  
 5 of measured natural crystals resembling more or less the 3D simulations with respective  
 6 projections.



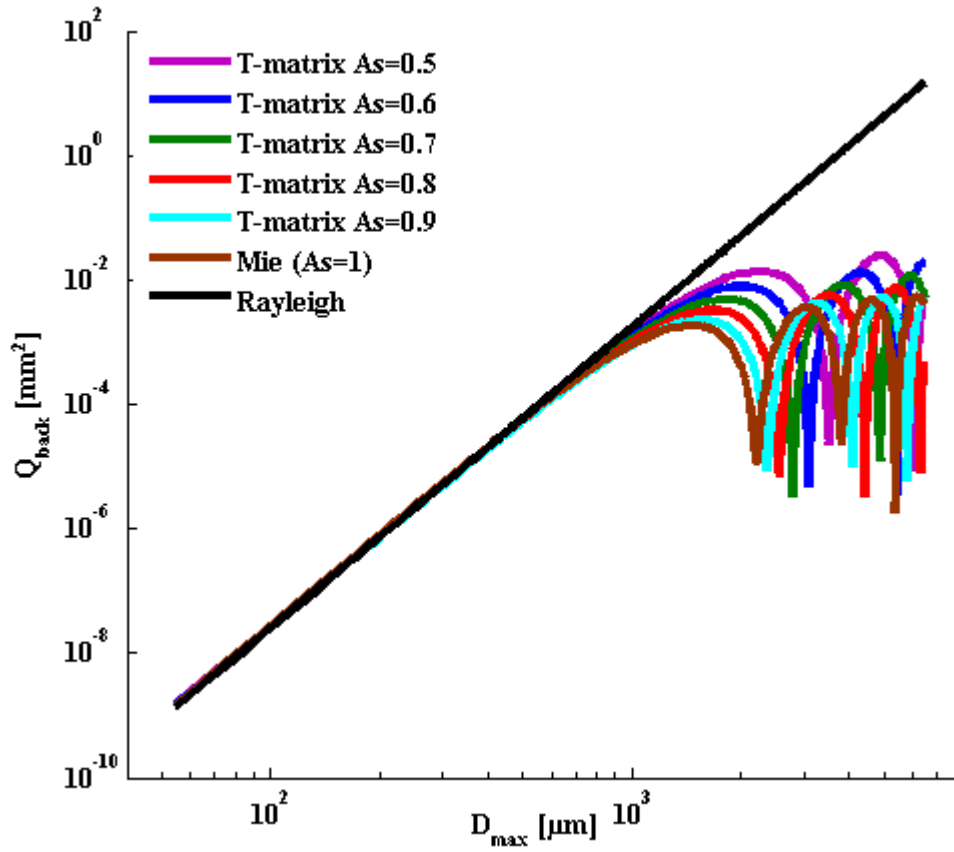
7  
 8 FIG. 4. Exponent  $\beta$  of  $m(D)$  relationship as a function of the exponent  $\sigma$  of the  $S(D)$   
 9 relationship. All data point either with red contours or without contours have been deduced  
 10 for a population of 1000 simulated 3D shapes and corresponding projections. Symbols with  
 11 red contours are deduced for 3D aggregates of crystals of an elementary shape. Symbols with  
 12 black contours stem from M96. The legend for symbols is given in Table 2. A linear fit of all

1 simulated data is shown by the black line. The grey band represents the mean standard  
2 deviation ( $\pm 0.16$ )

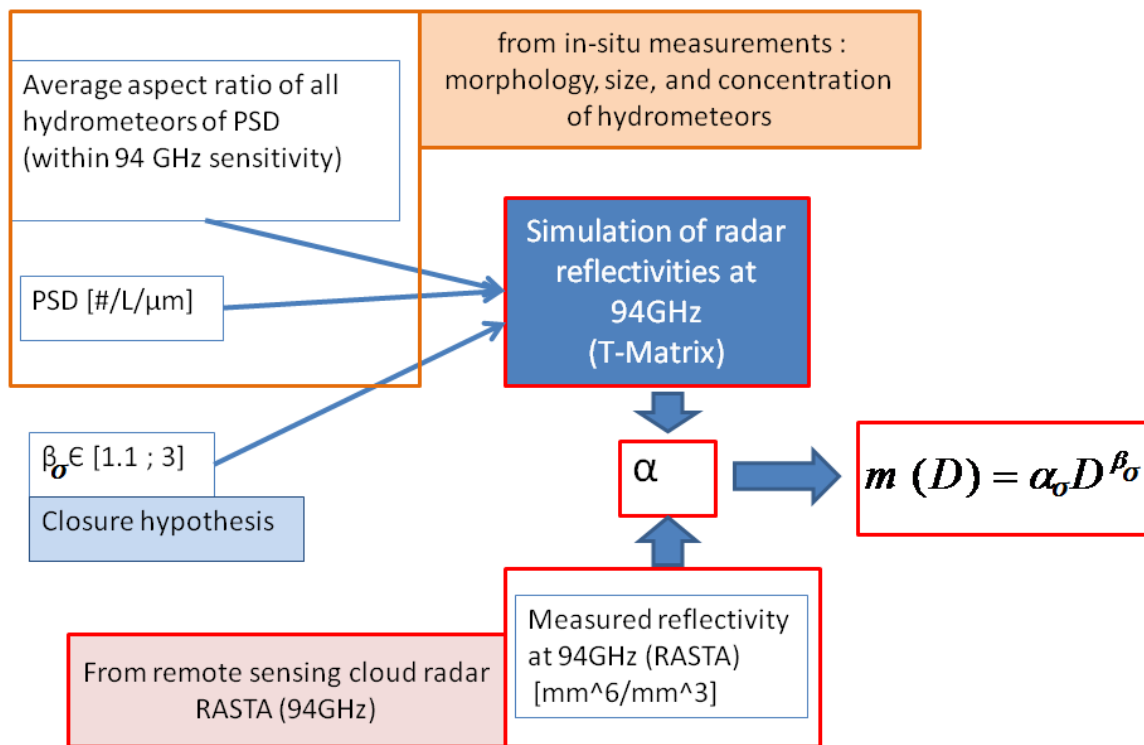


3  
4 FIG. 5. Mean projected surface versus Dmax. Black symbols represent the 2D-S image data  
5 and red symbols the PIP data. The grey line would be the power law fit for spherical particles.  
6 The golden line is the power law which fits the 2D-S data for  $D_{\text{max}}$  larger than  $250\mu\text{m}$  and the  
7 blue line fits the PIP data with a power law for  $D_{\text{max}}$  larger than  $950\mu\text{m}$ .

8  
9  
10



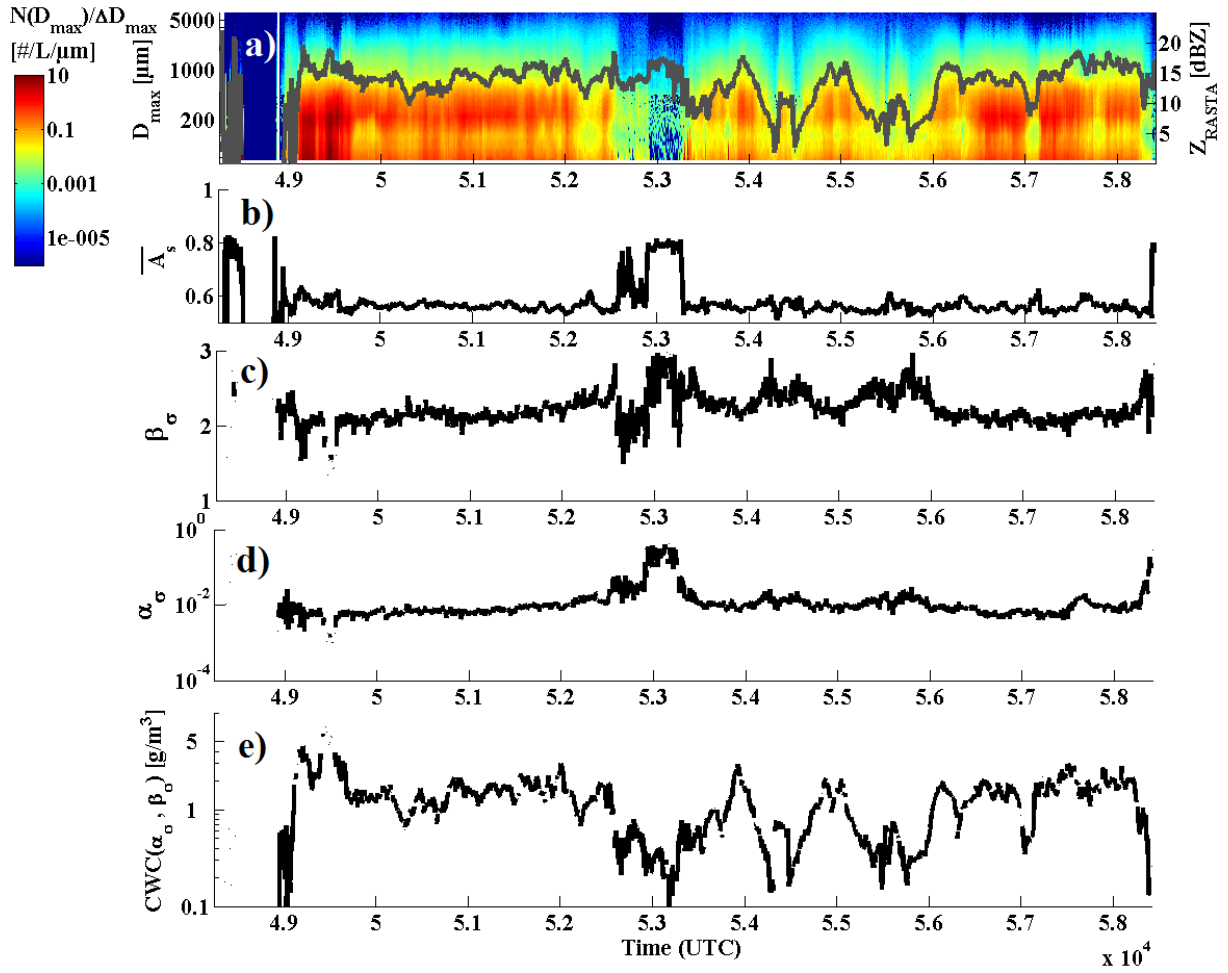
1  
2 FIG. 6. Calculated backscattering cross section as a function of the maximum particle  
3 diameter  $D_{max}$ . Pink, blue, green, red and cyan curves are calculated for different Aspect ratios  
4 by the T-matrix method, whereas the brown curve is based on the Mie theory calculation for a  
5 spherical particle. The black curve represents the Rayleigh approximation.  
6



1

2 FIG. 7. Implemented method to retrieve the coefficients (pre-factor and exponent) of the mass-  
 3 diameter relationship from the combination of radar reflectivity and 2D hydrometeor images.  
 4 Measured radar reflectivity and hydrometeor particle size distributions and average aspect  
 5 ratios serve as input for the T-matrix method used for reflectivity simulations for variable  $\beta_\sigma$   
 6 exponents. Closure hypothesis between measured and simulated reflectivities then yield the  
 7 pre-factor  $\alpha_\sigma$ .

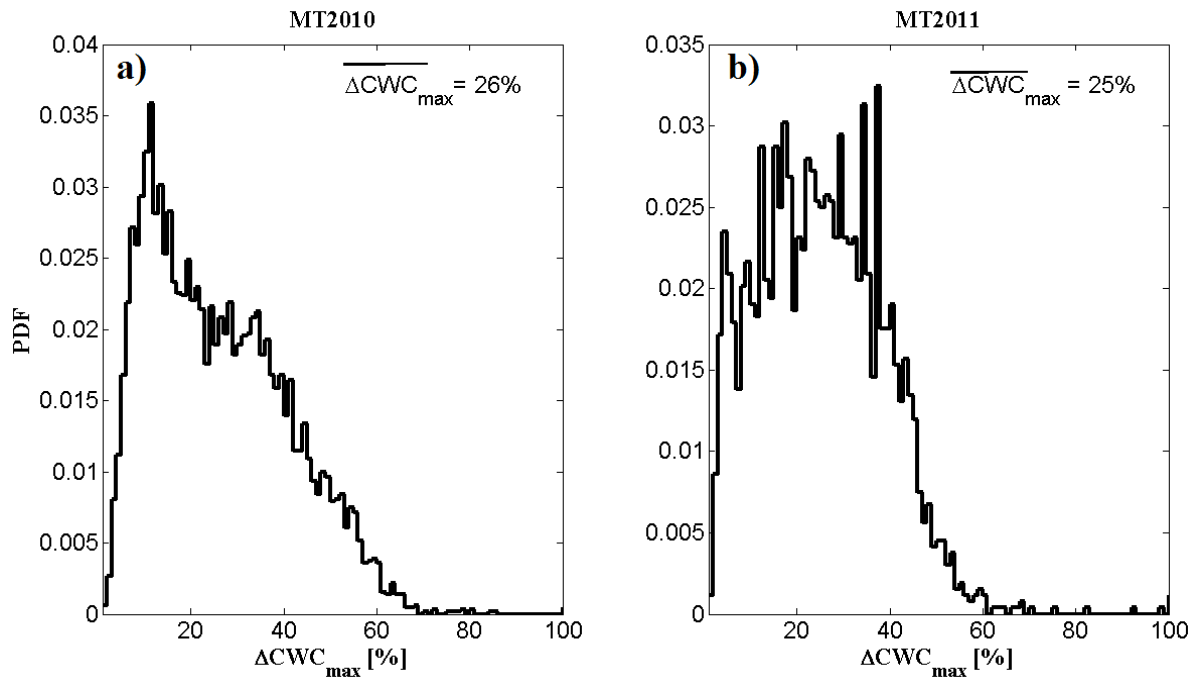
8



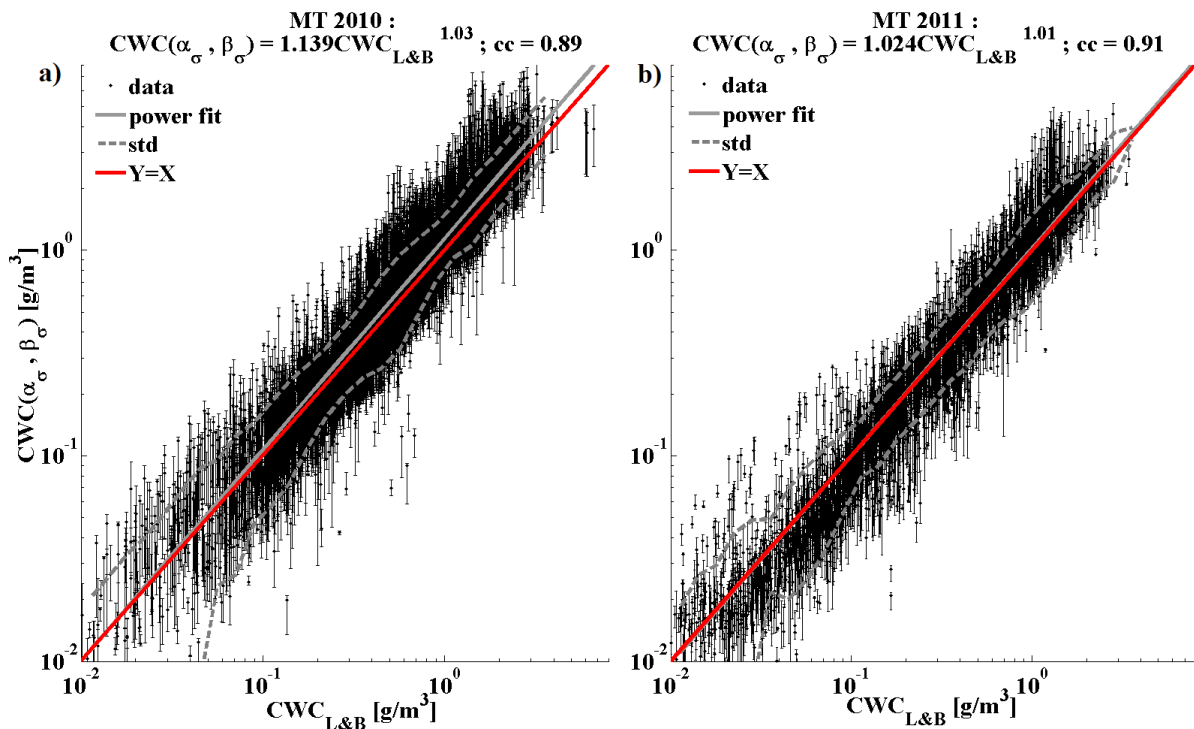
1

2 FIG. 8. (a) Contour plot of the time series of the number PSD (as a function of  $D_{\max}$ ) color  
 3 coded with the number concentration, the grey line shows the simultaneously measured radar  
 4 reflectivity (secondary y axis). (b) Mean aspect ratio along the flight. (c)  $\beta_\sigma$  exponent  
 5 calculated from  $\sigma$  according to equations 5 and 7. (d) Pre-factor  $\alpha_\sigma$ , subsequently deduced  
 6 with the T-Matrix method. (e) CWC calculated with  $\alpha_\sigma$  and  $\beta_\sigma$  presented above.

7



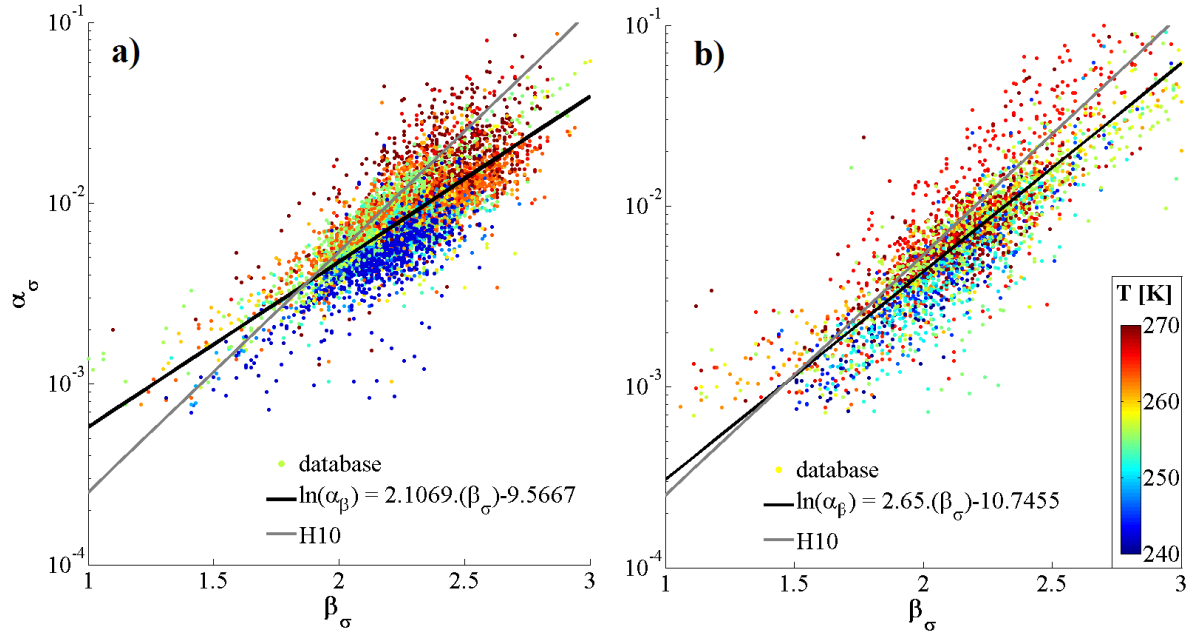
1  
 2 FIG. 9. Histograms of the maximum deviation ( $\Delta CWC_{max}$ ) on the retrieved CWC for a)  
 3 MT2010 and b) MT2011.



4  
 5 FIG. 10.  $CWC(\alpha_\sigma, \beta_\sigma)$  retrieved with T-matrix method including error bars versus  $CWC_{L\&B}$   
 6 calculated from Baker and Lawson (2006) for a) MT2010 and b) MT2011. Error bars  
 7 represent the minimum and the maximum of all possible CWC values, when  $\beta$  varies between

1 [1; 3]. The solid grey line represents a power law fit relating the two calculations. The dashed  
 2 grey lines represent the standard deviation and the red line represents a 1:1 relation between  
 3 CWC ( $\alpha_\sigma, \beta_\sigma$ ) and  $CWC_{L\&B}$ .

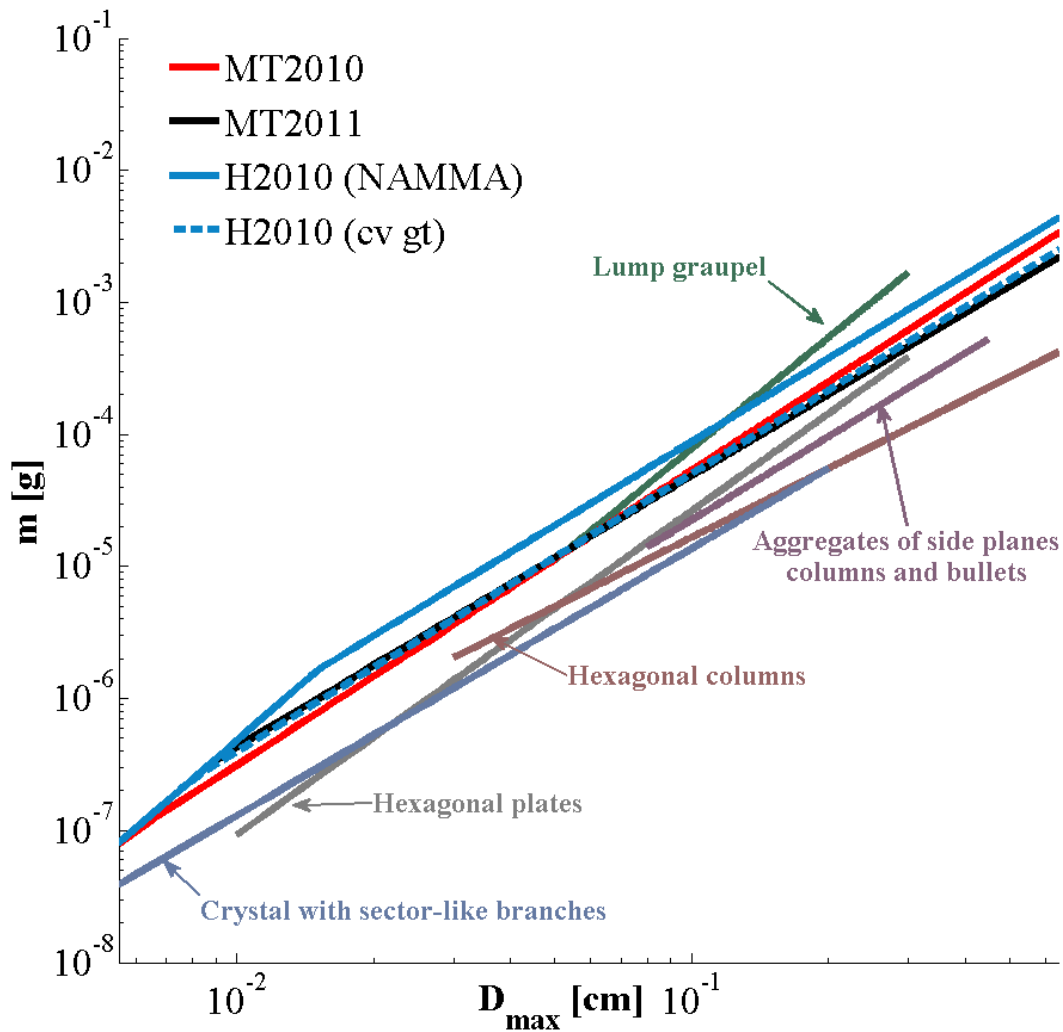
4



5

6 FIG. 11. Scatter plot of exponent  $\beta_\sigma$  as a function of  $\alpha_\sigma$ . Data points are color coded as a  
 7 function of temperature; black lines represent power law fits. The grey lines represent added  
 8 m(D) power law fits for CRYSTAL-FACE data from H10. a) MT2010 and b) MT2011.

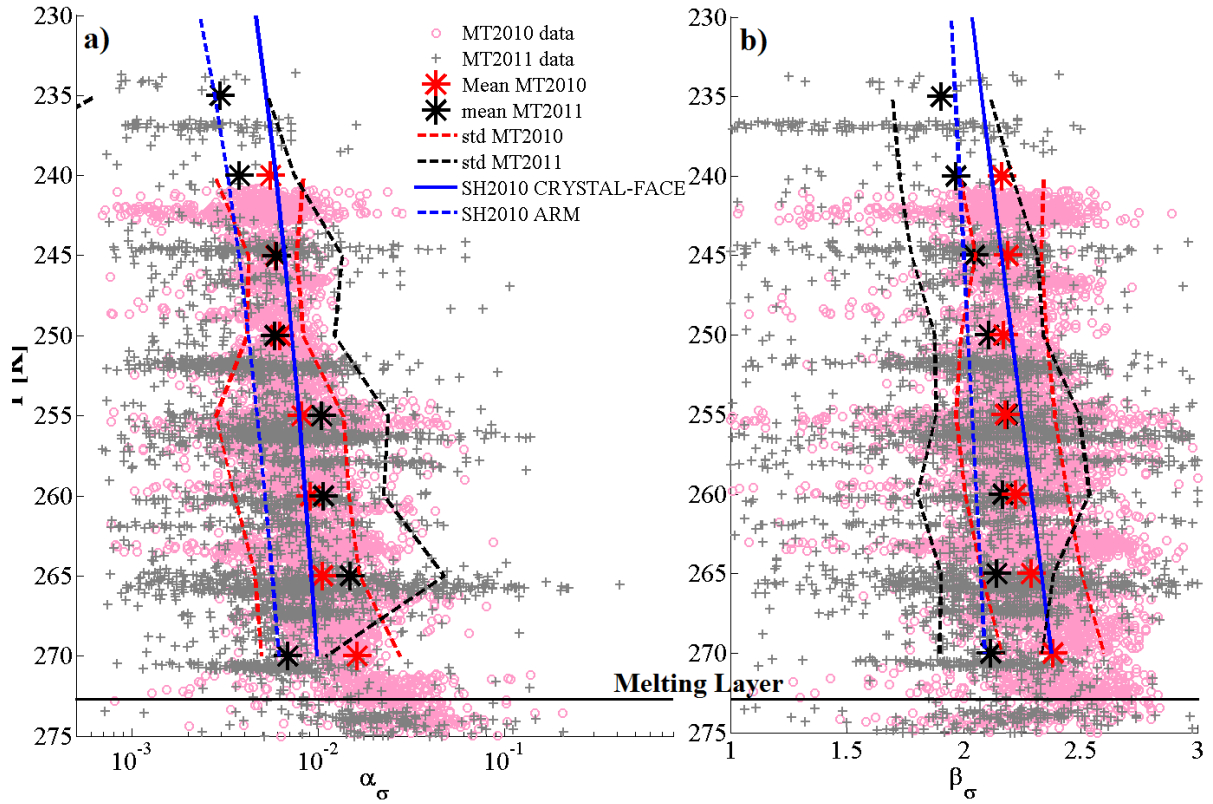
9



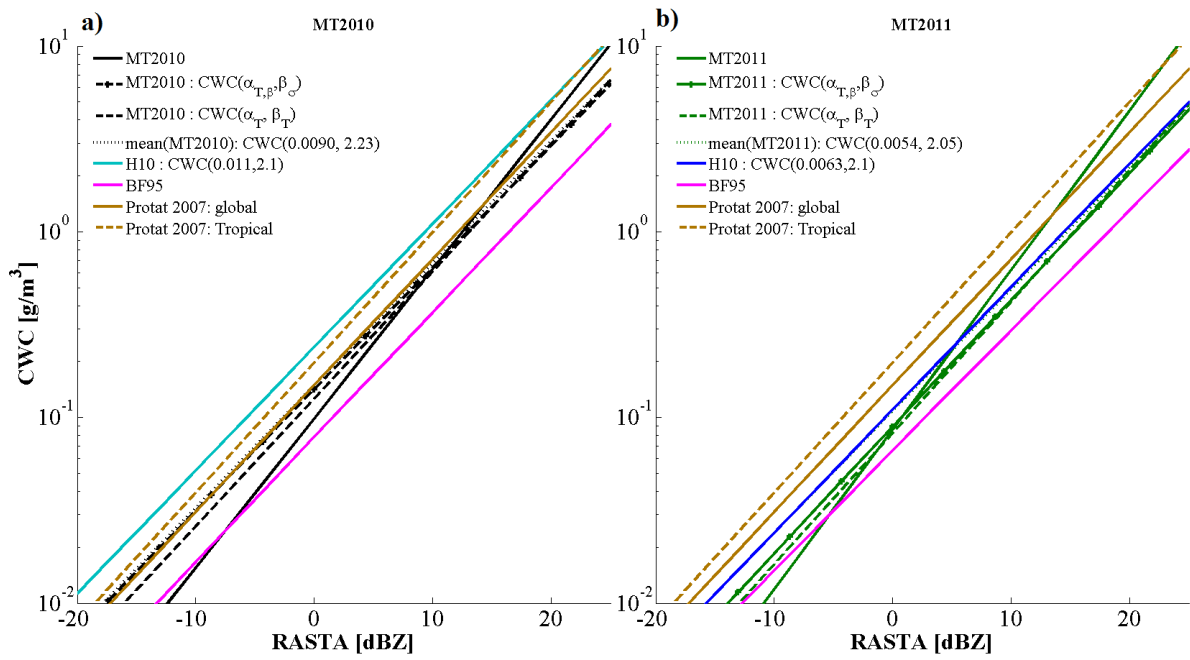
1  
 2 FIG. 12. Mass of individual ice crystals in gram as a function of their  $D_{\max}$ . The red line  
 3 represents mean values of  $m(D)$  coefficients for MT2010 (equation 19). Likewise, the black  
 4 dashed line represents  $m(D)$  coefficients for MT2011 (equation 20). The blue line represents  
 5  $m(D)$  coefficients taken from H10 for the NAMMA campaign and the dashed blue line also  
 6 stems from H10, but for convectively generated. Finally, various  $m(D)$  relationships are taken  
 7 from M96, as there are the blue-grey line for crystals with sector-like branches, the grey line  
 8 for hexagonal plates, the brown-grey line for hexagonal columns, the purple-grey line for  
 9 aggregates of side planes columns and bullets, and the green line for lump graupel.

10





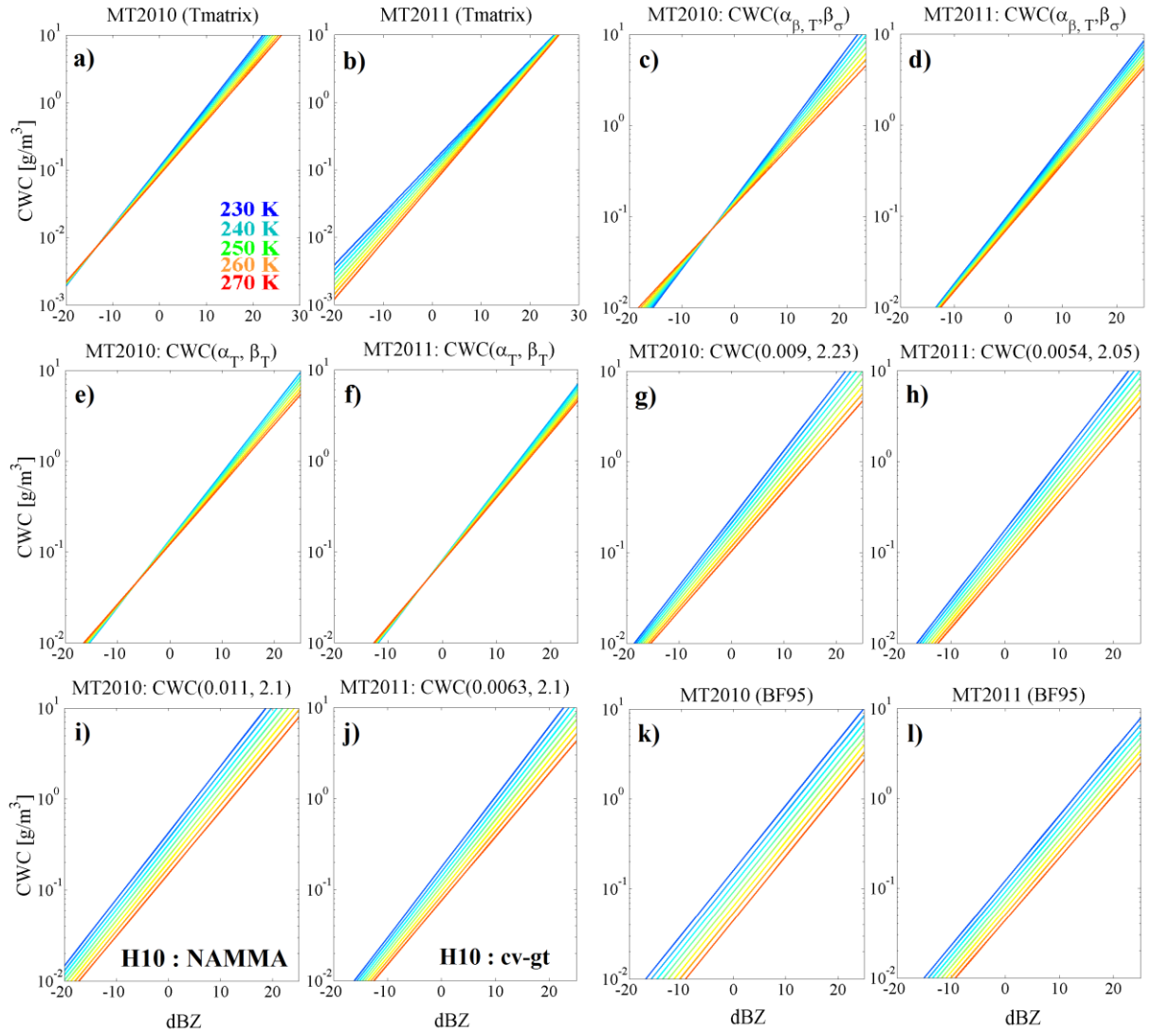
1  
 2 FIG. 13. Vertical variability of m(D) coefficients  $\alpha_\sigma$  and  $\beta_\sigma$ . (a)  $\alpha_\sigma$  versus the temperature in K.  
 3 (b)  $\beta_\sigma$  versus the temperature in K. Small symbols of pink circles show data points (5-seconds  
 4 time step) of MT2010, whereas grey crosses show MT2011 data. Large symbols of red and  
 5 black stars present mean values of m(D) coefficients in 5K temperature intervals for MT2010  
 6 and MT2011, respectively. Dashed red and black lines show standard deviations from the  
 7 mean value for MT2010 and MT2011, respectively. Blue solid and dashed lines show vertical  
 8 profiles of SH2010 obtained for CRYSTAL-FACE and for ARM campaigns, respectively.  
 9



1

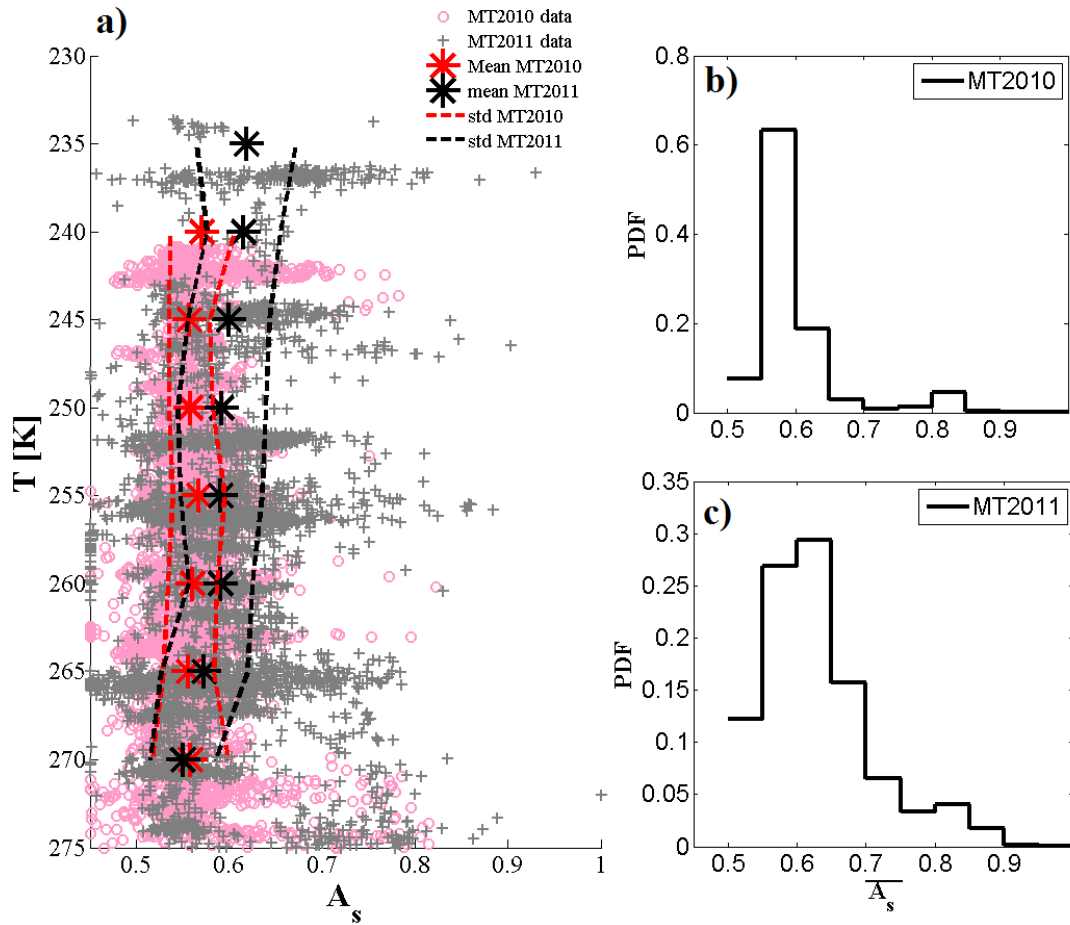
2 FIG. 14. Z-CWC fitted relationships between calculated CWC and measured radar reflectivities  
 3 for MT2010 and MT2011 datasets. Z is given in dBZ on the x axis and CWC in  $\text{g m}^{-3}$  on the y  
 4 axis. a) Power law fits for MT2010. b) Power law fits for MT2011.

5



1

2 FIG. 15. Z-CWC-T fitted relationships between calculated CWC and measured radar  
 3 reflectivities and temperatures for MT2010 and MT2011 datasets. Z is given in dBZ on the x  
 4 axis and CWC in  $\text{g m}^{-3}$  on the y axis. a) CWC are calculated from  $\alpha_\sigma$  and  $\beta_\sigma$  for MT2010  
 5 dataset. b) as for a) but for MT2011. c) CWC are calculated using  $\alpha_{\beta,T}$  and  $\beta_\sigma$  for MT2010  
 6 dataset. d) as for c) but for MT2011. e) CWC are calculated as a function of  $\alpha_T$  and  $\beta_T$  for  
 7 MT2010 (equation 21). f) as for e) but for MT2011 (equation 22). g) CWC are calculated  
 8 from average coefficient of MT2010 (equation 19). h) as for g) but for MT2011 (equation 20).  
 9 i) CWC are calculated using H10 m(D) coefficients of NAMMA for MT2010. j) CWC are  
 10 calculated using H10 m(D) coefficients of clouds convectively generated for MT2011. k)  
 11 CWC are calculated using the BF95 parametrisation for MT2010 dataset. l) as for k) but for  
 12 MT2011.

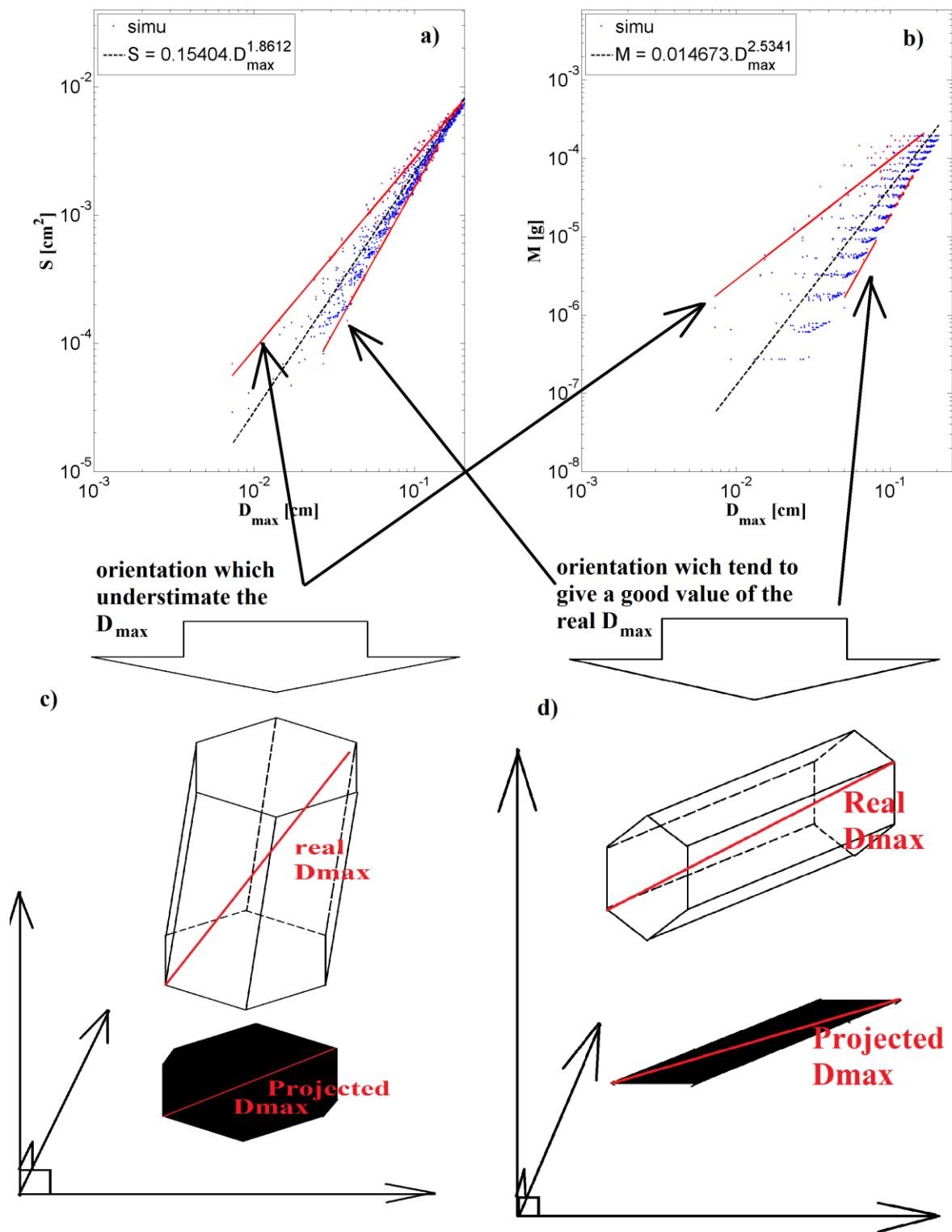


1

2 FIG. 16. a) Vertical profiles of the average aspect ratio  $\overline{A_s}$  as a function of temperature. Small  
 3 symbols of pink circles show data points (5-seconds time step) of MT2010, whereas grey  
 4 crosses show MT2011 data. Large symbols of red and black stars present mean values of  
 5  $\overline{A_s}$  in 5K temperature intervals for MT2010 and MT2011, respectively. Dashed red and black  
 6 lines show standard deviations for MT2010 and MT2011, respectively, from the average  
 7 value. b) Probability distribution functions of  $\overline{A_s}$  for MT2010. c) Probability distribution  
 8 functions of  $\overline{A_s}$  for MT2011.

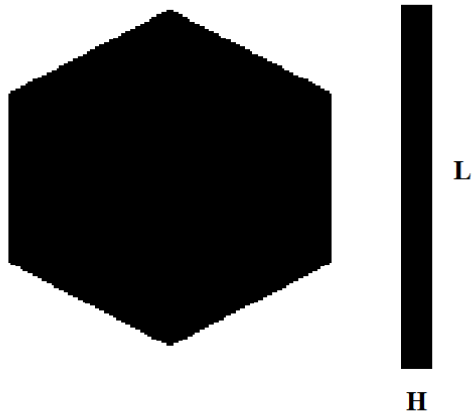
9

Simulations of Hexagonal Columns such  $L=0.2*H$



1  
 2 FIG. A1. Exemplary results obtained for a 3D simulation of columns characterized by  
 3 length=0.2\*height. a)  $S(D)$  plot: Blue points are the simulated data for the column, red lines  
 4 are power law fits enclosing most of the data points for all possible orientations. The dashed

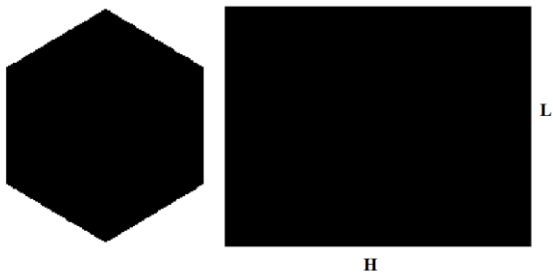
1 black line is the mean of the two power laws (= the mean between two red lines when the  
2 orientation underestimates  $D_{max}$  and when the orientation is close to the real  $D_{max}$ ). b)  $m(D)$   
3 plot: same as for a) but with the mass of the simulated columns which is now on the y-axis; c)  
4 Schematic of a 3D shape oriented in the 3D space when its orientation gives an  
5 underestimated value of the real  $D_{max}$  of the ice crystals. d) Schematic of a 3D shape oriented  
6 in the 3D space when its orientation gives a close value of the real  $D_{max}$  of the ice crystals.



7

8 FIG. A2. Schematic description of hydrometeors shapes for subsequent simulations of plates.

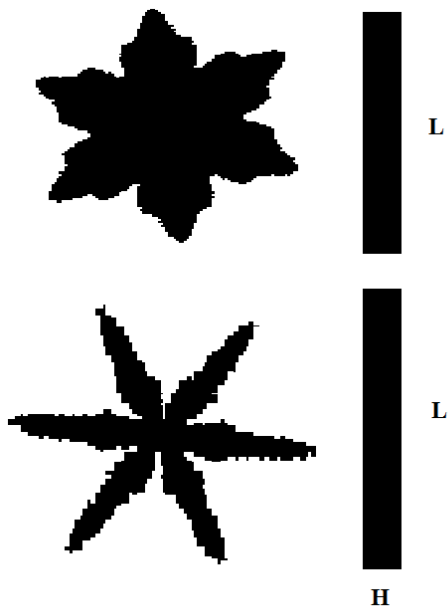
9



10

11 FIG. A3. Schematic description of hydrometeors shapes for subsequent simulations of  
12 columns.

13

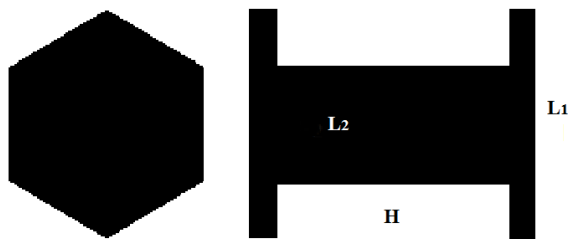


1

2 FIG. A4. Schematic description of hydrometeors shapes for subsequent simulations of slender  
 3 and solid stellars.

4

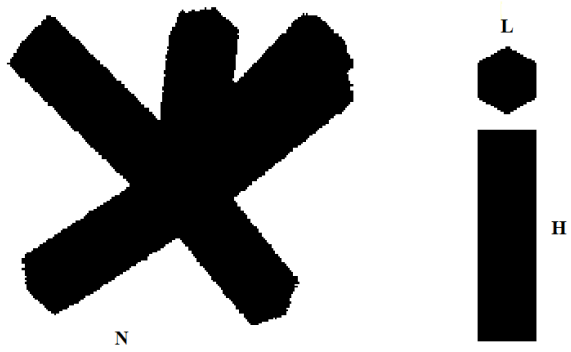
5



6

7 FIG. A5. Schematic description of hydrometeors shapes for subsequent simulations of capped  
 8 columns.

9



1

2 FIG. A6. Schematic description of hydrometeors shapes for subsequent simulations of bullet  
3 rosettes.



4

5 FIG. A7. Schematic description of hydrometeors shapes for subsequent simulations of  
6 aggregates of spheres.

7